QUARTERLY JOURNAL OF THE ROYAL METEOROLOGICAL SOCIETY

Effect of extreme ocean precipitation on sea surface elevation and storm surges

Journal:	*QJRMS*
Manuscript ID	QJ-15-0243.R1
Wiley - Manuscript type:	Research Article
Date Submitted by the Author:	09-Feb-2016
Complete List of Authors:	Wong, Benjamin; Imperial College London, Physics Toumi, Ralf; Imperial College London, Physics
Keywords:	ocean modelling, Cyclone Monica, rain mass, rain stress

Effect of extreme ocean precipitation on sea surface elevation and storm surges

Running head: Effect of extreme rainfall on sea surface elevation and storm surges

Benjamin Wong (corresponding author): benjamin.wong11@imperial.ac.uk

Ralf Toumi: r.toumi@imperial.ac.uk

Space and Atmospheric Physics Group,

Blackett Laboratory,

Imperial College London,

London SW7 2AZ,

UK

Keywords: ocean modelling, Cyclone Monica, rain mass, rain stress

Abstract

Ocean models that neglect mass and momentum contributions from precipitation can have a systematic bias in sea surface height (SSH). Here, a new rainfall scheme is introduced into the Regional Ocean Modelling System (ROMS) to incorporate the effects of precipitation mass. When precipitation is added to the sea surface, it spreads out via surface gravity waves that increase in propagation speed with increasing water depth. Over several days, the SSH increase due to the precipitation mass added created a geostrophic adjustment, generating anti-cyclonic geostrophic currents around the SSH increase. The transfer of momentum from precipitation to the sea surface, or rain stress, can also be important. In the case study of a real tropical cyclone, Monica passing North Australia, the effect of incorporating precipitation mass is compared with other processes affecting the storm surge: surface wind, inverse barometer effect and rain stress. The maximum SSH response is 170.6 cm for the wind effect, 61.5 cm for the inverse barometer effect, 7.5 cm for the effect of rain stress and 6.4 cm for the effect of rain mass. Each process has been shown to have different spatial influences. The effect of rain mass has a strong remote influence compared to the inverse barometer effect and the effect of rain stress. This is particularly seen in semi-enclosed bays.

1 Introduction

The contribution of oceanic precipitation to storm surges has so far been neglected in storm surge models, typically only incorporating the contributions of the inverse barometer effect (Roden et al., 1999) and wind driven effect towards the overall surge height. There is very little work addressing the contribution of oceanic precipitation to surge levels. This is expected, considering that many ocean models do not incorporate the mass and momentum effect of precipitation for it to be studied in detail. Sheng et al. (2012) described a test platform used to review several established storm surge models such as CH3D-SSMS (Sheng et al., 2010), ADCIRC (Westerink et al., 1992), FVCOM (Chen et al., 2008), CMEPS (Peng et al., 2004) and SLOSH (Jarvinen et al., 1985). Thirty scenarios were used to test their sensitivity towards parameters such as bathymetry, storm forcing, wind drag coefficient, bottom friction, Coriolis and 2D-3D formulation, but precipitation was not investigated. Ocean models such as ROMS (Shchepetkin et al., 2005) and FVCOM only incorporate the effect of temperature, salinity and momentum from rain, but not the effect of rain mass. Storm surge models such as ADCIRC and SLOSH ignore the effects of ocean rain entirely. Ponte (2006) incorporated realistic freshwater fluxes in a global barotropic model and found that they can cause annual standard deviations in sea surface level as large as 1 cm, especially in shallow and semi-enclosed regions. In highly precipitating storm events with extreme rain rates, the sea surface height increase may be more substantial. For instance, the highest rainfall recorded by Typhoon Morakot in 2009 was up to 74 cm day^{-1} (Wu, 2013). How this contributes to storm surges and to what extent rain mass can be neglected in this case is not known.

Here, a new rainfall scheme has been introduced into ROMS to account for the effect of rain mass. This scheme complements the existing rainfall routine in ROMS where only temperature and salinity changes due to rainfall are accounted for. An idealized set-up of ROMS will be used to isolate the effects of adding rain mass to the sea surface height. The Weather Research and Forecasting model (WRF, Skamarock et al., 2008) is used to generate the rain forcing to evaluate the sea surface height response in ROMS.

The transfer of momentum from raindrops to the water surface, or rain stress, was first documented by Van Dorn (1953), who concluded that the stress contributions from rainfall can considerably intensify surface stresses. Caldwell et al. (1970) have since built on his work, parameterizing rain stress as a function of rain rate and wind speed. This parameterization has been widely incorporated in many model studies such as the one-dimensional mixed layer model developed by Clayson et al. (1999) and the bulk parameterization outlined by Fairall et al. (1996) relating the near-surface atmospheric and the oceanographic bulk variables. This air-sea bulk parameterization has also been adopted in ROMS. While the parameterization of rain stress has been widely incorporated, there has been no study so far that shows its isolated effect in the models it has been implemented in. For the case of tropical cyclones, where extreme wind speeds and precipitation rates are found, the isolated effect of rain stress has not been shown and its contribution to storm surges is not known. This section shall employ the use of an idealised set-up in ROMS to show the isolated effects of rain stress in the context of storm surges.

Finally, a real case scenario is studied to compare the various processes affecting storm surges. Tropical Cyclone Monica (Durden, 2010) has been chosen for her high wind speed, low system pressure and high rainfall, which are the key storm surge effects investigated here. A validated atmospheric state is generated using WRF and is prescribed onto ROMS to investigate how various processes affect the storm surge. The significance of rain mass and rain stress is compared with two other established storm surge processes: the inverse barometer effect and the effect of surface wind. Each of these physical effects is investigated based on their isolated contribution to the total SSH and storm surge patterns.

2 Model set-up and validation

2.1 Set-up of idealized case

Rain mass is introduced to ROMS through a new rainfall scheme that incorporates rain rate as point sources. This approach is similar to how river run-off is introduced to the model, but in this case, vertical fluxes are added instead of horizontal fluxes. The rainfall rate from the atmospheric rain forcing is converted into point sources without further prescribing its temperature and salinity. The temperature and salinity of rain is accounted for within the existing bulk flux routine where air-sea momentum and energy exchanges are calculated (Fairall et al., 1996). An idealized set-up of ROMS is used to create a controlled environment, isolating the specific effects investigated here. The ROMS grid is set up with closed boundaries, a horizontal resolution of 15 km, 21 vertical levels and a spatial extent 5°N to 35°N and 120°E to 180°E. The initial ocean state has a uniform temperature of 26°C and salinity of 35 psu. The land mask is specified at the western boundary up to 140°E to simulate the coastline. A third-order upwind scheme is used for horizontal momentum advection, and a Smagorinsky-like viscosity is applied (Griffies et al., 2000). The turbulence closure scheme used to calculate vertical mixing is based on the Generic Length Scale (GLS) parameterization as described by Umlauf et al. (2003).

An idealized tropical cyclone is simulated using WRF and prescribed onto ROMS. The set-up of the initial cyclone profile and atmospheric state follows Wang et al. (2015). For the WRF simulation, one single nest is set up with 31 vertical levels and a horizontal resolution of 15 km in the domain spanning 5°N to 35°N and 120°E to 180°E. The microphysical parameterization used is based on Lin et al. (1983). Cumulus parameterization is not included, which reduces the computational time required for each simulation. Without cumulus parameterization, the amount of precipitation may be underestimated at a 15 km horizontal resolution. However, the aim of this part of the study is to understand the specific effect of adding precipitation mass to the ocean model in a simple, idealized set-up, and not to reproduce the atmospheric domain with high accuracy. The surface layer scheme is based on Monin-Obukhov, with Zilitinkevich thermal roughness length and standard similarity functions (Paulson, 1970). Planetary boundary layer processes are parameterized using the Mellor-Yamada-Janjic scheme (Janjic, 1994). The longwave and shortwave radiation schemes are implemented from Mlawer et al. (1997) and J. Dudhia (1989) respectively.

2.2 Rain stress parameterization

In ROMS, rain stress is implemented in the bulk fluxes routine from Fairall et al. (1996) and based on the parameterization by Caldwell and Elliott (1970) as follows:

$$\tau_{rx} = 0.85 R \rho_r |\vec{v}_{10}| * SIGN(U_{10}) \qquad (1)$$

$$\tau_{ry} = 0.85 R \rho_r |\vec{v}_{10}| * SIGN(V_{10}) \qquad (2)$$

where R is the rain rate, ρ_r is the density of rainwater, τ_{rx} is the rain stress in the x direction, $SIGN(U_{10})$ denotes the sign of U_{10} (U-component wind speed at 10 m), τ_{ry} is the rain stress in the y direction and $SIGN(V_{10})$ denotes the sign of V_{10} (V-component wind speed at 10 m).

The rain stress parameterization of Caldwell and Elliott (1970) is derived from a one-dimensional model where $\vec{v}_{10}$ refers to the wind velocity in the direction of reference. When considering wind velocity resolved into its orthogonal components, it would be incorrect to utilize the total velocity in calculating the rain stress. Here, the magnitude of the u-component winds (U) and the v-component winds (V) used in the calculation of rain stress will always be $\sqrt{U^2+V^2}$. This results in a systematic overestimation in the magnitude of rain stress by a factor of $\sqrt{2}$. The error in the direction of rain stress is more inconsistent. Since U and V are always set to be equal in magnitude (equal to the net wind speed), the directions of the rain stress can only be in any of the four directions: 45°, 135°, 225° and 315°, unless there is zero rainfall or zero wind speed. Furthermore, the existing ROMS rain stress code always assigns a positive sign to zero values. For example, if U is zero, it will still be assigned the magnitude of V (now equal to the magnitude of the net wind speed), with the direction of positive U. The error in the direction of the rain stress term can range from 0° (when U=V) to 45° (when either U=0 or V=0). Overall, this results in a systematic overestimation of rain stress and an incorrect direction calculated for the overall wind stress.

The corrected implementation of the rain stress parameterization is as follows:

$$\tau_{rx} = 0.85 R \rho_r U_{10} \tag{3}$$

$$\tau_{ry} = 0.85 R \rho_r V_{10} \tag{4}$$

An idealized set-up of ROMS is used to verify the corrected implementation of rain stress. Here, the u-component wind is set to a constant -1 m s^{-1} and the v-component wind is set to zero. One centimetre of rain is introduced to a single cell (15 km by 15 km) in the centre of the domain (20°N 150°E) at the first hour. Two simulation runs are conducted to compare the existing implementation of rain stress (using equations (1) and (2)) with the corrected implementation of rain stress (using equations (3) and (4)). Both simulation runs are subtracted from a control run without any rain stress to eliminate any noise such as the SSH response to the background u-component wind.

2.3 Set-up of real case

The ROMS set-up uses a single grid at a horizontal resolution of 6 km, with the open boundaries using the Flather (1976) conditions for the barotropic velocities and the Chapman (1985) conditions for sea surface elevation. A minimum depth of 10 m and maximum depth of 5500 m has been specified. Twenty layers are chosen in the vertically stretched terrain-following sigma-coordinate, with higher resolution placed at the surface and lower resolution placed at the bottom. Geometry of the bathymetry is obtained from Global Topography v14.1 (Smith, 1997). The tidal forcing is applied at the open boundaries and imposed on the elevation and the barotropic velocities. It is derived from 11 tidal harmonics that are extracted from the 1/12° resolution Pacific Ocean Atlas solution provided by the Oregon State University (OSU) Tidal Data Inversion (Egbert et al., 1994). A nudging relaxation zone with eight grids from the boundary is set up to relax the baroclinic structure to the forcing fields at the boundary (Marchesiello et al., 2001). The 1/12° resolution HYbrid Coordinate Ocean Model (HYCOM) (Bleck et al., 1981) global daily analysis data is used as the initial, boundary and nudging conditions for the model.

The pressure-driven effect in ROMS is obtained by applying the atmospheric pressure field from WRF and the sea level is adjusted based on the inverse barometer approximation (Gill and Niiler, 1973). The inverse barometer effect is generally a good approximation for sea level responses to local atmospheric pressure. For non-isostatic pressure effects, Hirose et al. (2001) found that deviations from the inverse barometer effect contributed only up to 2 cm in large-scale basins such as the Pacific and Atlantic Ocean. For smaller-scale basins such as Cape of Carpentaria, the non-isostatic deviation was under 0.5 cm and is much smaller compared to the precipitation effects in this case (Figure 10b).

WRF is used to simulate a high resolution atmospheric state of tropical cyclone Monica to be prescribed onto the ocean model for the case study. Two nests are employed with 28 vertical levels. The final grid has a horizontal resolution of 6 km. NCEP Climate Forecast System Reanalysis (CFSR) (Saha et al., 2010) has been used for initial and lateral boundary conditions. The boundary forcing is prescribed every 6 hours and the model interior is allowed to evolve freely. The ETA scheme (Rogers et al., 2001) is chosen for microphysical parameterization. The Kain-Fritsch cumulus parameterization scheme (Kain, 2004) has been used for both nests. The surface layer scheme is based on Monin-Obukhov with Carslon-Boland viscous sub-layer and standard similarity functions. The selected planetary boundary layer is from Yonsei University (Hong et al., 2006). The Mesoscale Model 5 (MM5) 5-layer thermal soil temperature model (Dudhia, 1996) is used to calculate the heat and moisture fluxes over the land. The longwave and shortwave radiation schemes are implemented from Mlawer et al. (1997) and Chou et al. (1994) respectively.

The isolated effects of including precipitation mass source, rain stress, inverse barometer effect and surface wind forcing are individually investigated by comparing with four separate configurations that are simulated with precipitation mass source, without rain stress, without the inverse barometer correction and without surface wind forcing respectively. The five experiments conducted are tabulated in Table 2.1. Spatial plots of SSH are differenced from the control simulation (Case A) to illustrate the isolated effects of each process.

Cases	*WRF wind conditions applied to ROMS*	*Inverse barometer effect in ROMS*	*Rain stress effect in ROMS*	*New rain mass scheme*
Case A	Wind forcing applied	Turned ON	Turned ON	NOT used
Case B	NO wind forcing applied	Turned ON	Turned ON	NOT used
Case C	Wind forcing applied	Turned OFF	Turned ON	NOT used
Case D	Wind forcing applied	Turned ON	Turned OFF	NOT used
Case E	Wind forcing applied	Turned ON	Turned ON	In use

Table 2.1: Cases set up with different ROMS model options and wind conditions.

3 Results

3.1 Idealized case: response to rain mass

An idealized set-up of ROMS is used to study the effect of rainfall mass on sea surface elevation. The effect of rainfall is isolated by setting the wind field to zero and all other atmospheric forcings are set to a constant nominal value. Rain is introduced to a single grid cell (15 km by 15 km) at 20°N 150°E for 1 hour at the rate of 1 cm/h, to understand the effect of a single-point perturbation on the free surface. Figure 1 shows the ocean surface response after 2 hours and 9 hours. The illustrations are zoomed into the area 9°N to 31°N and 134°E to 176°E. A surface gravity wave is generated, propagating radially outwards from the point of perturbation. At time = 1 h, the maximum SSH is 0.0181 cm and the minimum is -0.0076 cm. At time = 9 h, the maximum SSH is 0.0043 cm, the minimum is -0.0045 cm and the wave propagates to about 10° from the initial point of perturbation. Over 9 hours, the amplitude of the gravity wave drops by about 76%.

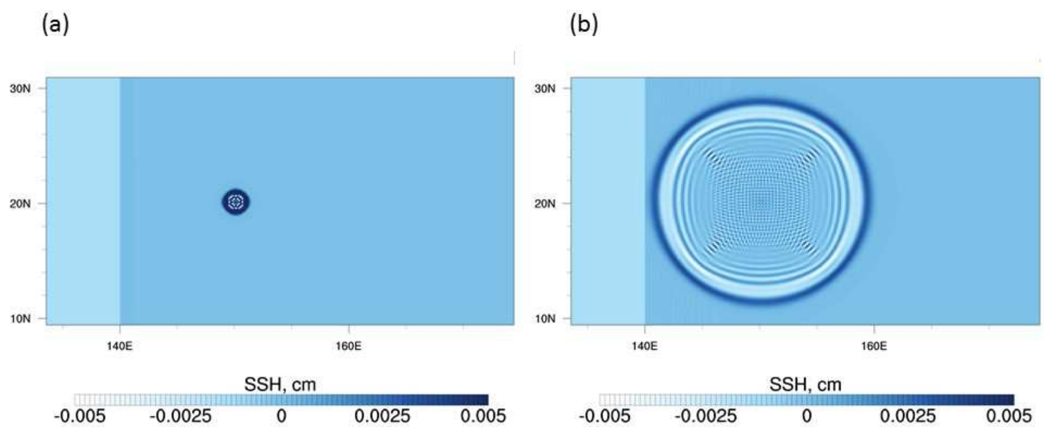

Figure 1: SSH response to rain mass addition to a single surface grid cell after (a) 1 hour and (b) 9 hours. Land is west of 140°E, ocean is east of 140°E. Wind forcing is set to zero.

Next, the SSH response to rainfall at a longer time scale is studied by forcing ROMS with rainfall from an idealized tropical cyclone simulated using WRF over 8 days. The maximum rain rate is not at the centre of the cyclone, but along the rain bands. As the cyclone treks from the east to the west of the domain, it gradually grows in size and intensity. The rain bands of the tropical cyclone also increase in size with time. Figure 2 shows the cumulative rainfall throughout the event, with a maximum of 319 mm at any one grid. To avoid any interference from the winds, the wind field is set to zero so the sea surface is unaffected by wind stress and responds only to the cyclone rainfall.

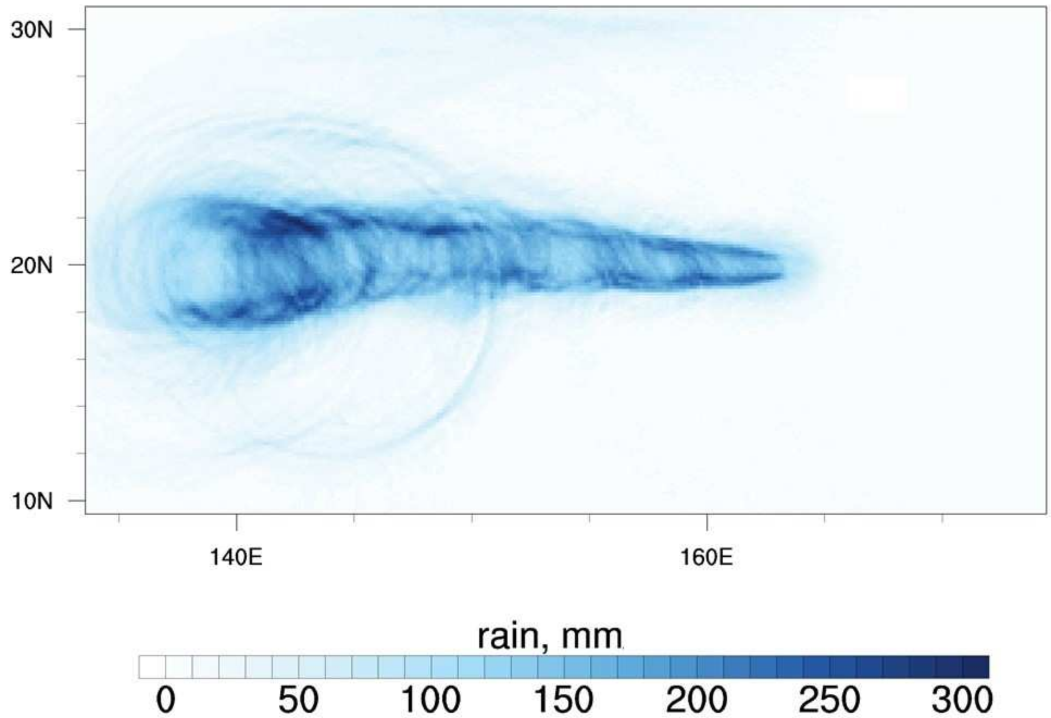

Figure 2: Cumulative rainfall of the idealized tropical cyclone over 8 days.

The SSH response to rainfall from the idealized tropical cyclone is simulated for two ocean depths at 100 m and 1000 m deep. Figure 3 shows the SSH at the 170th hour of the simulation when the tropical cyclone makes landfall at the coastline along 140°E. For both depths, the SSH increases along the rainfall path and gradually decreases towards the domain boundaries. For the case with a depth of 100 m, the maximum SSH is 5.8 cm and the minimum SSH is 1.3 cm at the 170th hour. A clockwise gyre is formed, with the sea surface currents at a magnitude of 10^{-2} m s^{-1}. For the case with a depth of 1000 m, the maximum SSH is 3.2 cm while the minimum SSH is 2.3 cm. A weaker clockwise gyre is formed with the sea surface currents at a magnitude of 10^{-3} m s^{-1}.

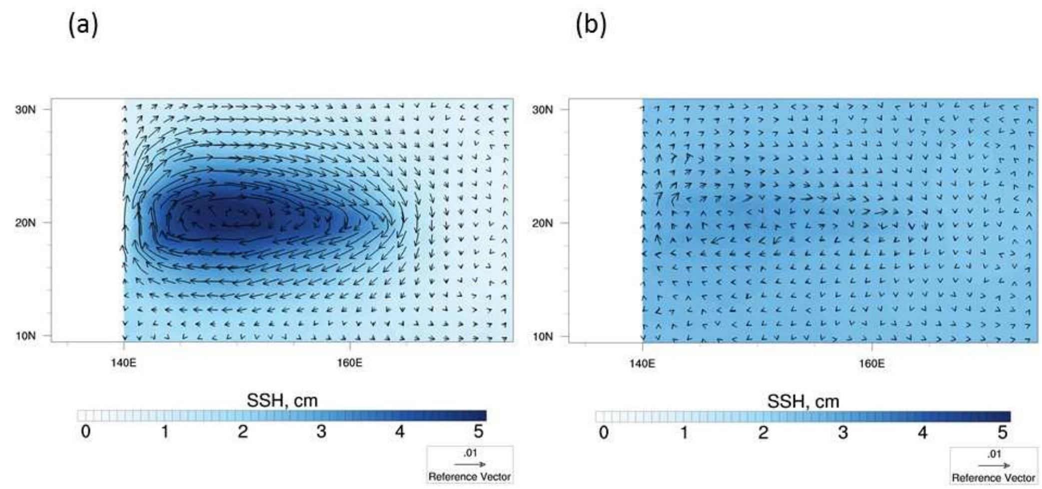

Figure 3: SSH and sea surface current response to the rain mass added to the ocean with (a) 100 m depth and (b) 1000 m depth at the 170th hour.

3.2 Idealized case: response to rain stress

Figure 4 shows the rain stress perturbation setting off a surface gravity wave that propagates outwards from the point of perturbation towards the domain boundaries. Two implementations are shown for the existing and the corrected model. In the existing implementation of rain stress (Figure 4a), the resulting surface gravity wave is at an angle of 45° to the wind direction. The front of the wave is led by a crest in the north-westward direction with an amplitude of up to 0.01 cm. In the south-eastward direction, the wave is led by a trough of up to 0.01 cm in amplitude. Figure 4b shows the SSH response to the corrected implementation of rain stress in ROMS. The surface gravity wave generated from the rain stress perturbation is now symmetrical to the wind direction. In the westward direction, the front of the wave is led by a crest of up to 0.005 cm in amplitude. In the eastward direction, the wave is led by a trough of up to 0.005 cm in amplitude.

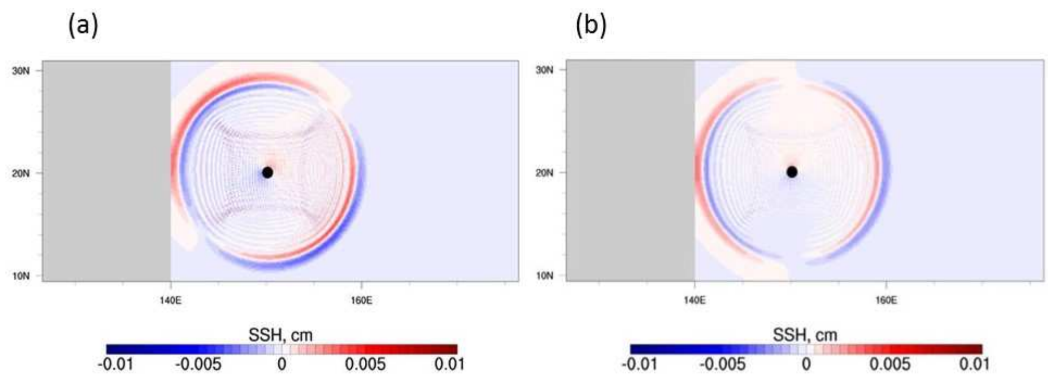

Figure 4: Sea surface height at 10 hours after introducing a rain stress perturbation for (a) the existing implementation of rain stress in ROMS and (b) the corrected implementation of rain stress in ROMS. The black dot in the centre of the domain (20°N 150°E) denotes the initial position of perturbation. Wind forcing is set to zero.

Next, the contribution of rain stress to storm surges is investigated by forcing ROMS with an idealized tropical cyclone simulated using WRF. Here, the wind and rainfall fields are retained, but the other forcing fields are set to a nominal and constant value in order not to introduce interfering signals into the system. To show the isolated effect of rain stress, the response of SSH and sea surface currents from the rain stress simulation was subtracted from a control simulation (Figure 5). Here, an anticlockwise circulation centering 20°N 141°E is generated with a decrease in SSH at the circulation centre. The positive surge is up to +0.44 cm and the negative surge is up to -0.63 cm.

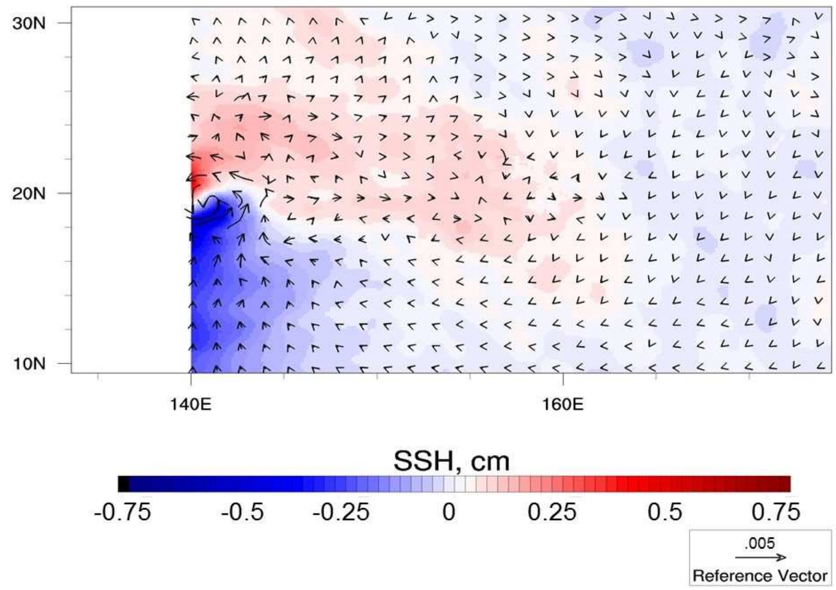

Figure 5: Response of SSH and sea surface currents to rain stress at t = 163 h.

3.3 Case study: validation of Cyclone Monica

The atmospheric state is simulated for the period between 20 April 2006 and 24 April 2006. Minimum sea level pressure from WRF is used to generate the cyclone path for comparison as shown in Figure 6. This cyclone path is validated using the storm track provided by the Australian Bureau of Meteorology (BOM, http://www.bom.gov.au/cyclone). On 20 April 2006, both the modelled cyclone and the observed cyclone are located at the western coast of Cape York Peninsula, but the modelled cyclone is situated more northwards compared to the observed cyclone. The modelled path is largely similar to the observed path, but has a northward offset of up to 1°. The modelled cyclone also travels faster than the observed cyclone by up to a day.

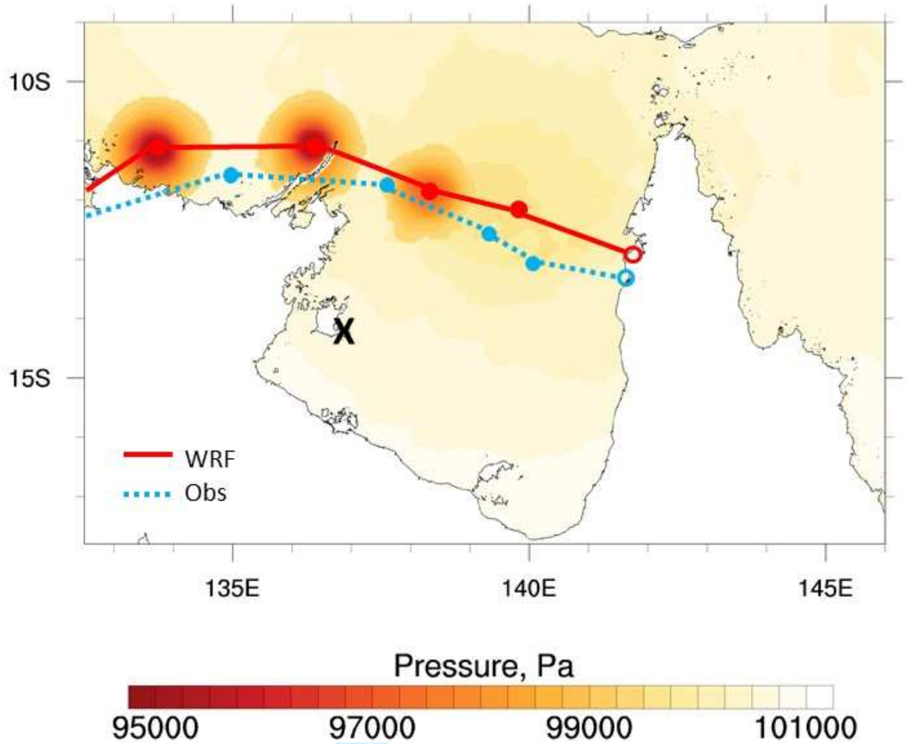

Figure 6: Cyclone path of WRF (solid line) and observations from BOM cyclone report (dashed line). Filled circles are positions every 24 hours from 0000 UTC 20 April 2006 (open circle). Location of the Groote Elyandt weather station is indicated with an 'X'.

Based on the observed weather conditions provided by BOM, the maximum wind speed observed at Cape Wessel (11°S, 136.8°E) and Maningrida (12°S, 134.2°E) were 130 km h^{-1} and 148 km h^{-1} respectively. In WRF, the maximum modelled wind speed at Cape Wessel and Maningrida were 141 km h^{-1} and 146 km h^{-1} respectively, which compared well with observations (Figure 7).

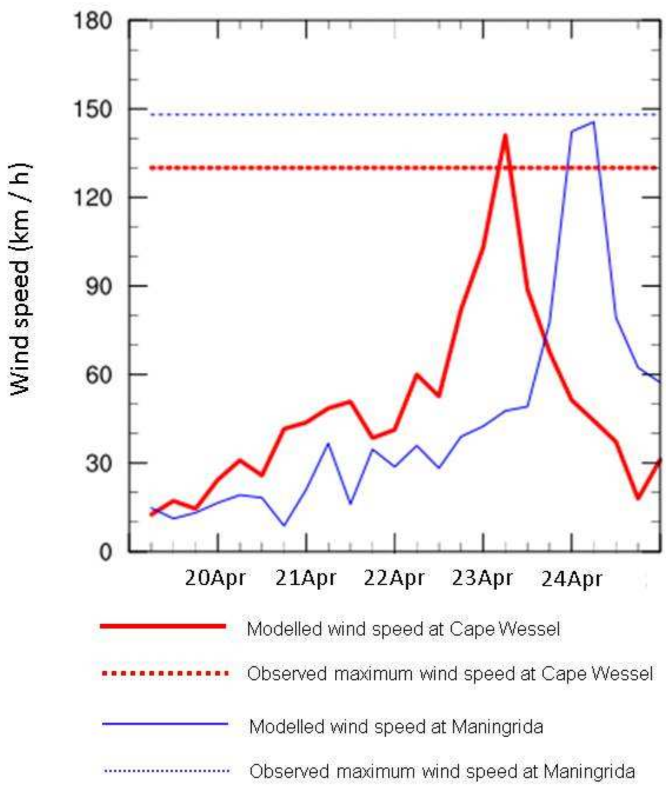

Figure 7: Comparison of the modelled wind speeds at Cape Wessel (11°S, 136.8°E) and Maningrida (12°S, 134.2°E) with the maximum wind speeds observed.

The simulated precipitation is compared with the multi-satellite rainfall estimates from the Tropical Rainfall Measuring Mission (TRMM) 3B42 version 6 (Huffman et al., 2007) (Figure 8). The modelled rainfall path is largely in line with the observed rainfall path but the rainfall is more intense along the cyclone track and less intense away from the track. The observed cumulative rainfall (TRMM) is more homogeneous, having more regions with 100 – 300 mm of rainfall. Nevertheless, the domain cumulative rainfall in WRF is 6% more than that observed by TRMM, although this percentage is expected to be higher since the WRF rainfall is summed with the land mask applied, while TRMM rainfall is summed over every cell in the domain. The total domain cumulative rainfall simulated using WRF is 4.7 x 10^6 mm and the observed cumulative rainfall in TRMM is 4.4 x 10^6 mm over 8 days. However, this is not a large concern in this case study since the main objectives are to simulate and compare various processes in a realistic environment and not to closely replicate the exact storm event. The precipitation rates modelled here are not uncommon among tropical cyclones in Australia and similar storm systems in other parts of the world. From the BOM reports on historical tropical cyclones, the highest observed precipitation rates of Monica was 340 mm day^{-1}, Laurence (December 2009) at 402 mm day^{-1}, Paul (March 2010) at 443 mm day^{-1} and Yasi (January 2011) at 471 mm day^{-1}. Outside of Australia, the estimated maximum rainfall of Hurricane Katrina (August 2005) was 300 mm day^{-1} (Dodla et al., 2011) and Typhoon Morakot (August 2009) was 741 mm day^{-1} (Wu, 2013). Hence, the rainfall produced by Monica is not an extreme case compared to other tropical cyclones and the overestimation in the rainfall simulated here does not lead to an unrealistic scenario.

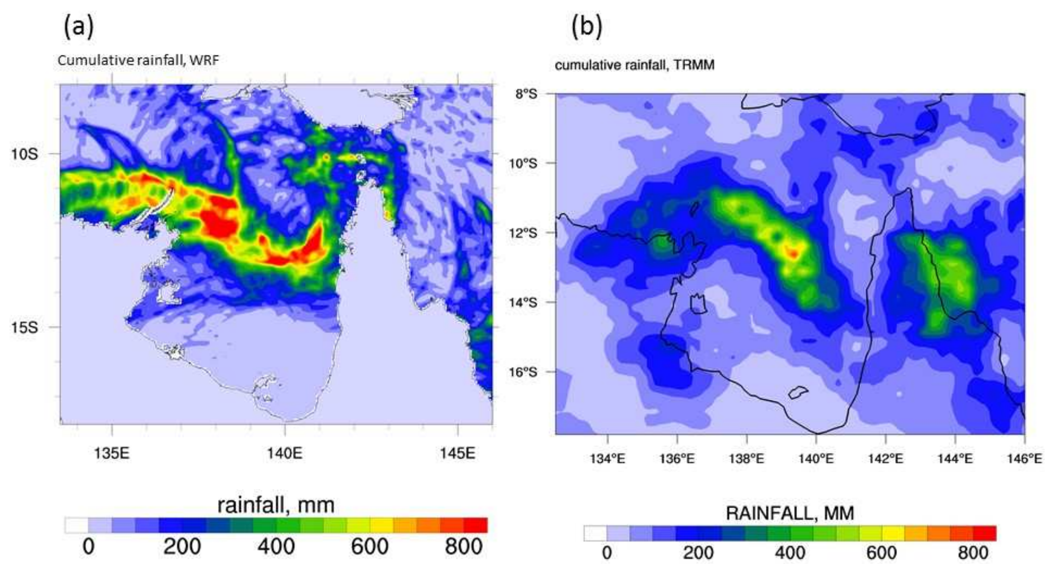

Figure 8: 8-Day cumulative rainfall output from 19 April 2006 for (a) WRF and (b) TRMM.

The configuration of ROMS used for validating the ocean state incorporated the effects of rain mass, rain stress, the inverse barometer effect and all atmospheric forcings including wind. The storm surge (Figure 9) is validated against the tidal gauge measurements taken from Milner Bay in Groote Elyandt. The tidal gauge data is obtained from the Australian Baseline Sea Level Monitoring Project (ABSLMP) (Watson, 2011). To compare the storm surge, the tidal components are detided using the tidal package by Codiga (2011). The tidal range is very large and there remains a residual tidal-like signal after de-tiding eleven tidal components that were introduced into ROMS in the tidal forcing set-up. At this location, the surge simulated in ROMS (23 April 2006) is earlier than the observed data (24 April 2006) by a day. However, the magnitude of the surge is very well-captured. The difference in modelled and observed time of peak surge is also consistent with the different translation speed and track of the WRF cyclone. The modelled cyclone is located north of the Groote Elyandt station around 1200 UTC 22 April 2006, while the observed cyclone reaches north of the Groote Elyandt station around 0000 UTC 24 April 2006. However, the modelled cyclone path is situated more north compared to the observed cyclone path and a longer time is expected for the storm surge to be picked up at Groote Elyandt. Hence, an overall difference of a day can be expected between the modelled and observed storm surge.

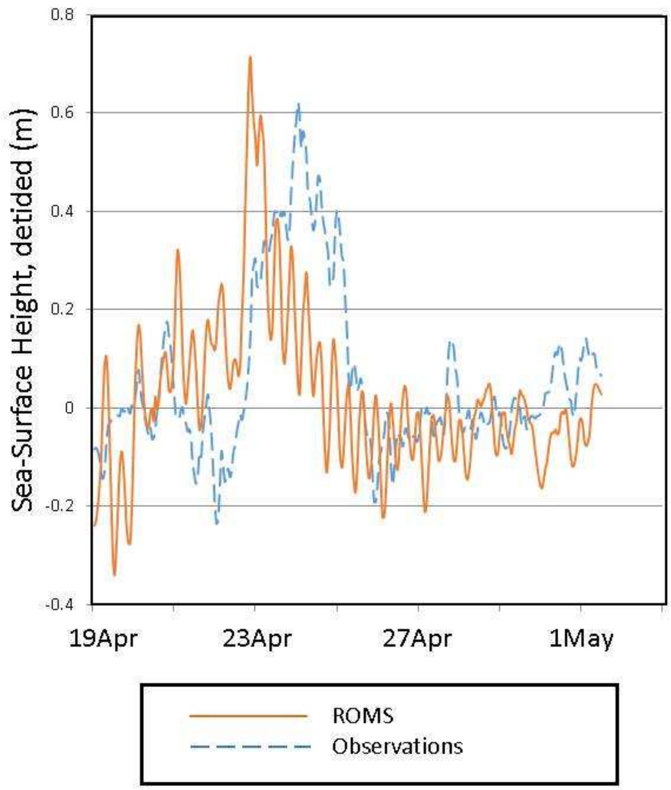

Figure 9: Comparison between the storm surge generated in ROMS with tidal gauge measurements (detided) at Groote Elyandt weather station obtained from ABSLMP, with the location indicated with an ‘X’ on Figure 6.

3.4 Case study: contribution of rain to SSH

We examine the individual contributions to the SSH response to Cyclone Monica. The SSH response to the effect of wind (Figure 10a) is the largest compared to the other effects. On 21 April 2006, the negative surge is up to -58 cm at the south-eastern boundary of the Gulf of Carpentaria and the positive surge is up to 61 cm on the western boundary. On 22 April 2006, the negative surge at the south-eastern boundary of the gulf and the positive surge at the western boundary still persist. There is a region of negative SSH located at the centre of the gulf. The minimum SSH is -57 cm and maximum SSH is 60 cm. On 23 April 2006, the cyclone reaches the Wessel Islands and the SSH rises up to 171 cm in Buckingham Bay (12°S 136°E). The positive surge at the western boundary of the gulf is still present at this time, but the negative surge at the south-eastern boundary has reverted to its nominal levels. At the northern coast of the Arnhem Land, the negative surge is up to -111 cm.

Figure 10b shows the SSH change due to the inverse barometer effect. The SSH increase is localized to the position of the cyclone and increases as the cyclone intensifies through the event. The distribution of the SSH scalar field is similar to atmospheric pressure, with the highest SSH at the centre of the cyclone, gradually decreasing with distance from the cyclone centre. The SSH increases from 13 cm on 21 April 2006 to 61.5 cm on 23 April 2006 as the cyclone intensifies.

The additional SSH response due to the effect of rain stress is shown in Figure 10c. On 21 April 2006, the additional negative surge is up to -2.4 cm on west coast of Cape York Peninsula. There is an additional positive SSH of up to 0.9 cm near the position of the cyclone centre. On 22 April 2006, when Monica is at the centre of the Gulf of Carpentaria, there is an additional positive SSH of up to 0.7 cm ahead of the cyclone and a negative SSH of up to -1.1 cm behind the cyclone. On 23 April 2006, there is an additional positive surge of up to 7.5 cm to the east of the Wessel islands and an additional negative surge of up to -2.9 cm to the west of the islands.

Figure 10d shows the additional SSH response due to rain mass, increasing as the cyclone tracks across the Gulf of Carpentaria and decreasing when the cyclone passes. On 21 April 2006, Monica is situated at the western coast of Cape York Peninsula and the SSH rises up to 3.7 cm at the coast. On 22 April 2006, Monica is centred in the gulf and the SSH increases up to 4.6 cm, spreading out to the rest of the gulf. The sea level at the southern boundary of the gulf increases up to 3.5 cm. On 23 April 2006, the cyclone reaches the Wessel Islands and the SSH rises up to an additional 6.4 cm. The sea level change at the southern boundary of the gulf decreases to 2 cm.

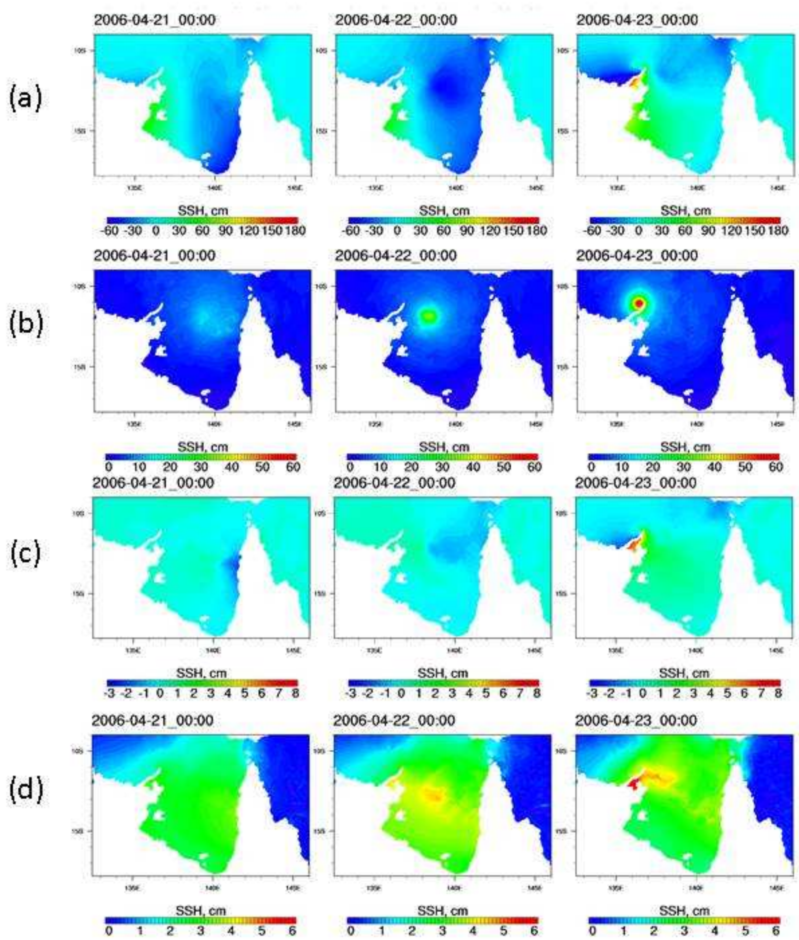

Figure 10: Additional SSH response to the effect of (a) wind, (b) atmospheric pressure, (c) rain stress and (d) rain mass from 21 April 2006 to 23 April 2006.

4 Discussion

The rain mass perturbation on the water surface sets off a surface gravity wave propagating outwards towards the domain boundaries over a time scale of several hours (Figure 1).

Characteristics of surface waves are inherently non-linear. But considering shallow water approximations (Stewart, 2009), where the water depth is much smaller than the wavelength, the phase speed (c) can be expressed as:

$$c = \sqrt{gd} \tag{5}$$

where g is the gravitational acceleration and d is the depth of water.

From the initial point of perturbation, the surface wave propagated from 20°N 150°E to 20°N 160°E in 9 hours translating at a speed of 30.9 m s^{-1}. The shallow water approximation is valid for water depths much lesser than the wavelength. Here, the water depth is 100 m while the wavelength is about 100 km. The water depth in this case is only 0.1% that of the wavelength, making the shallow water approximation a valid assumption. From equation (5), the surface gravity wave in this case should advance at a phase speed of 31.3 m s^{-1}, which is consistent with the ROMS output.

Next, the SSH response at a longer time scale is examined using an idealized tropical cyclone to force the ocean model over 8 days. In Figure 3, the added mass spreads outwards from the mass sources towards the domain boundaries via gravity waves. In the deeper ocean case, the maximum SSH is smaller (up to 3.2 cm) compared to the shallow ocean case (up to 5.3 cm). From equation (5), gravity waves in the deeper case travel 3 times faster than in the shallow water case, which accounts for the faster decrease in the maximum SSH for the deeper ocean case. With the rain mass spreading out faster in the deeper ocean, the minimum SSH reaches a higher level for the deep ocean case (2.3 cm) compared to the shallow ocean case (1.3 cm). At longer time scales (after 7 days), a pressure gradient is generated from the sea surface height increase. This creates a geostrophic adjustment with an opposing Coriolis force. Geostrophic currents of the magnitude 0.01 m s^{-1} are generated, rotating in a clockwise direction.

With the implementation of rain stress now corrected in ROMS, the SSH response to rain stress is shown by forcing ROMS with an idealized tropical cyclone (Figure 5). Rain stress is parameterized as a function of rain rate and wind speed and follows the direction of the winds. Hence, rain stress is only exerted in areas where non-zero values of rain rate and wind speed coincide. In the case of a tropical cyclone, rainfall is highest along the rain bands towards the centre of the cyclone. Rain stress contributes to storm surges in a manner similar to wind stress. The anti-clockwise rotating rain stress creates an anti-clockwise gyre at the sea surface. Coriolis force deflects the currents to the right and generates an outward diverging flow that decreases the SSH at the centre of the gyre.

Finally, a real case study is investigated to compare the SSH response to different storm surge processes. The effect of wind (Figure 10a) is the largest compared to the effect of precipitation and the inverse barometer effect. It drives positive and negative SSH anomalies based on the wind direction and the geometry of the coastline. On 21 April 2006, the strong easterly wind to the south of the domain generates a positive surge at the western boundary of the Gulf of Carpentaria due to the onshore wind. A negative surge is generated at the south-eastern boundary of the gulf due to the offshore wind. On 22 April 2006, the easterly wind to the south of the domain continues to generate a positive and negative surge at the western and south-eastern boundaries of the gulf respectively. There is a SSH depression in the middle of the gulf due to Ekman pumping. This SSH depression is present in all the 6-hourly output from 1800 UTC 21 April 2006 to 1800 UTC 22 April 2006 when Monica is trekking across the Gulf of Carpentaria. The SSH depression is absent on 21 April 2006 and 23 April 2006 when the cyclone is near Cape York Peninsula and the Wessel Islands respectively. On 23 April 2006, the cyclone is relatively far from the eastern boundary of the gulf and the offshore winds here weakens from the range of 15 m s^{-1} (21 April 2006) to the range of 10 m s^{-1}. The negative surge at the eastern boundary of the gulf weakens correspondingly. On the other hand, the positive surge at the western boundary of the gulf strengthens with the strong onshore winds. At this time, the strong winds blowing into Buckingham Bay create a funnelling effect, channelling water into the bay and generating a high positive surge of up to 171 cm.

The SSH response to the inverse barometer effect is spatially constrained by the location of the cyclone's low pressure centre and varies in magnitude based on the storm intensity (Figure 10b). SSH is expected to increase by 1 cm for every 1 mbar drop in atmospheric pressure (Roden & Rossby, 1999). The inverse barometer effect contributes substantially to the storm surge when the low pressure centre of the cyclone coincides with the coastline. When the cyclone is away from the coastline and over the open sea, the inverse barometer effect raises the SSH but does not contribute significantly to the storm surge. On 21 April 2006, Monica crosses the west coast of Cape York Peninsula but due to its low intensity at this time, the contribution to the storm surge is only up to 13 cm. On 22 April 2006, the storm intensifies as it crosses the Gulf of Carpentaria but due to its distance from the coast, the contribution to the storm surge is only around 10 cm, despite raising the SSH up to 35.2 cm in the centre of the gulf. On 23 April 2006, Monica intensifies further, crossing the Wessel Islands and increases the storm surge by up to 61.5 cm.

A region is subjected to rain stress when rainfall and winds coincide. On 21 April 2006, the location of intense rain is situated just off the west coast of Cape York Peninsula (Figure 10c). The cyclone is traversing westward with an overall westward wind direction. Rain stress perturbation on the sea surface creates a positive front ahead of the perturbation and a negative front behind it as shown in Figure 4. The offshore winds and high rainfall at the eastern boundary of the gulf generates a SSH response to rain stress, enhancing the negative surge here. While the wind stress generated positive and negative surges at the western and south-eastern boundaries of the Gulf of Carpentaria, these surges are absent in the rain stress effect shown here due to the lower rainfall at these locations. On 22 April 2006, the cyclone is in the middle of the gulf trekking westwards. This creates a similar effect with the positive SSH ahead of the cyclone and a negative SSH behind it. The positive and negative surges at the western and south-eastern boundaries of the gulf are similarly absent here, due to the light rainfall in these areas. On 23 April 2006 when the cyclone crosses the Wessel Islands, the effect of rain stress is very similar to that of wind stress, with the intense rain coinciding with the strong winds here. The additional positive surge in Buckingham Bay is generated due to rain stress channelling water into the bay, which is similar to the effect of wind stress. At the northern coast of the Arnhem Land just west of the Wessel Islands, the offshore winds coincide with the high rainfall from the storm to generate an offshore rain stress and a negative surge of up to -2.9 cm.

Figure 10d shows the SSH response to precipitation mass addition. From 21 April 2006 to 22 April 2006, the areas of SSH change do not confine solely to the precipitation footprint (as traced out in Figure 8a), but spreads out, advecting to the south of the Gulf of Carpentaria. On 23 April 2006, the cyclone crosses the Wessel Islands and the rain mass is trapped in Buckingham Bay, generating an additional local SSH increase of 6.4 cm. The effect of precipitation is essentially an in-situ addition of mass, and inlets and semi-enclosed basins will serve to enhance this effect by trapping the rain. Buckingham Bay is fairly well-resolved in this 6 km resolution model, spanning 13 x 14 grid cells, so the size of the effect is unlikely to be just numerical. The geometry of the gulf itself is an important contributing factor towards the effect of precipitation seen here. From Figure 10d, it can be seen that the SSH response is generally higher to the southern half of the gulf than the north. If the gulf was entirely enclosed, the additional mass will be expected to distribute evenly by the clockwise gyre in both the northern and southern regions. The constrained southern boundary of the gulf enhances the build-up of SSH within the gulf, since the north-western section of the gulf opens up to the Arafura Sea. Typical remote enhancements are of the order of 2 cm.

Evaporation, often considered in tandem with precipitation, can have notable effects on sea surface elevation. Roden et al. (1999) have reported oceanic evaporation to be between 0.08 cm day^{-1} to 0.55 cm day^{-1}, depending on wind conditions. Hurricane evaporation rates have been found to be in the order of 1 – 2 cm day^{-1} (Riehl and Malkus (1958), Machta (1968), etc). At this order of magnitude, the evaporation rate is much smaller compared to the effect of rainfall in this case, with local effects of up to 14 cm (mass and momentum transfer). Nevertheless, it will be interesting to include the effect of evaporation rate on sea surface height in future work for a comprehensive comparison.

The Gulf of Carpentaria is not an isolated case of a semi-enclosed basin that is prone to severe storms and many other cases have been studied. Zhong et al. (2010) used ROMS to study the storm surge predictions during the passage of Hurricane Isabel in Chesapeake Bay and found that the hurricane translation speed and the resolution of the horizontal wind field are important factors affecting storm surges. Rego et al. (2010) used FVCOM to simulate Hurricane Ike at Galveston Bay and found that the Bolivar Peninsula provided a significant surge barrier in protecting the bay. Westerink et al. (2008) developed a model of south Louisiana (which included many inlets, bays and channels) using ADCIRC to simulate the effect of storm surges during the events Hurricane Betsy and Andrew. Weisberg et al. (2006) used FVCOM to simulate the storm surge produced from several idealized hurricanes crossing Tampa Bay and found that the hurricanes with slow transitional speeds produced larger surges within the bay. However, none of these studies or models include the effect of rain mass. The semi-enclosed bay comprising Buckingham Bay, extending to the Wessel Islands and Gove Peninsula (12°2'S 136°5'E) consists of about 250 cells, which is equivalent to an area of 9000 km^2. The areas investigated in literature, such as Tampa Bay (5700 km^2), Galveston Bay (1600 km^2) and Chesapeake Bay (11600 km^2) are all of similar sizes or smaller. Not including the effect of rain mass in the models used in these studies will imply a systematic error in the storm surge levels modelled.To further compare how each of the physical effects contribute to coastal impacts in a worst case scenario, the SSH at the coastline starting from the Wessel Islands and ending at the northern tip of Cape York Peninsula is investigated. The maximum storm surge (for the duration of the storm) due to each physical effect is shown against the coastal locations (Figure 11) to illustrate the worst case scenario that can arise from each effect during this event. Considering the maximum storm surge response to the different processes at each coastal point, the additional effect of rain mass ranges from 1.3 cm to 6.4 cm, the effect of rain stress is from 0.4 cm to 7.5 cm, the inverse barometer effect is from 0.2 cm to 45.4 cm and the effect of wind stress is from 20.5 cm to 170.6 cm. While the inverse barometer effect is generally larger than the effect of rain mass, it falls below the effect of rain mass at the southern boundary of the gulf (coastal points 180 – 330) when the cyclone is located away from the coastline. This shows that the effect of rain mass can have a stronger remote presence than the inverse barometer effect. Although the maximum surge level due to the effect of rain stress is higher than the effect of rain mass, the effect of rain mass is larger than the effect of rain stress in most of the coastal points. ROMS (and many ocean models) include the effect of rain stress but not the rain mass even when the effect of rain mass can be larger as shown here. Ocean models that consider the effect of rain stress to be sufficiently substantial to include its effect should not neglect the effect of rain mass.

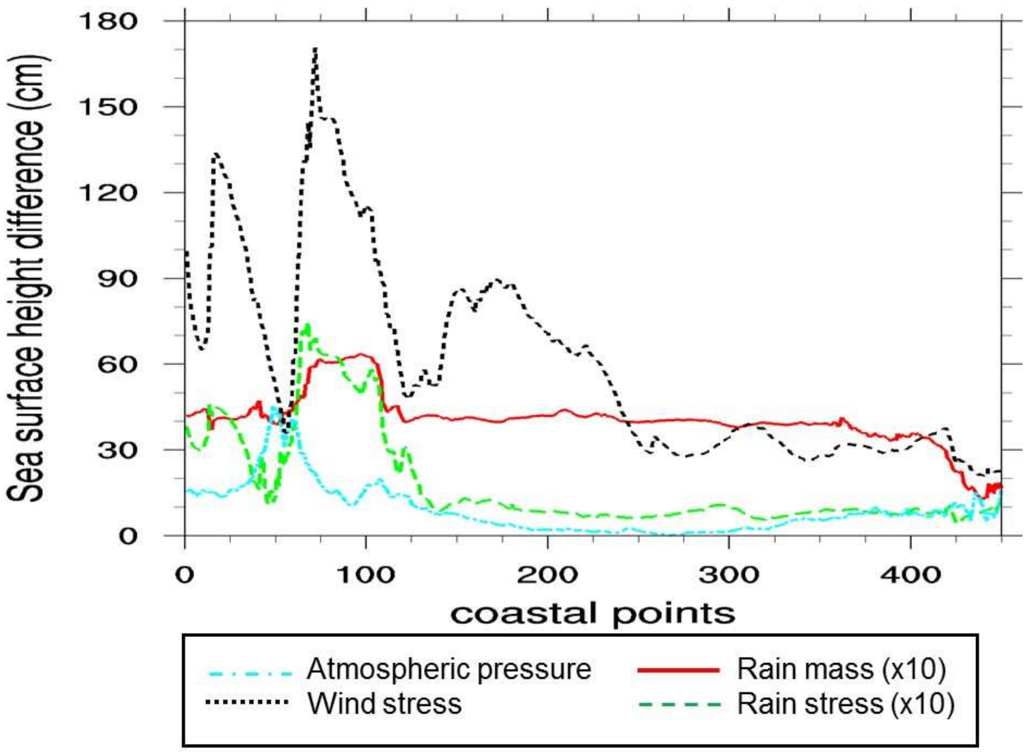

Figure 11: Comparison of the SSH change due to various physical effects, along the coastline at Gulf of Carpentaria. The coastal points can be attributed to different locations along the coastline as follows: the Wessel Islands (points 1 – 120), the western boundary of the Gulf of Carpentaria (points 121 – 180), the southern boundary of the gulf (points 181 – 280) and the eastern boundary of the gulf (points 281 – 450). SSH responses to rain mass and rain stress are scaled up by a factor of 10 for illustration.

5 Conclusion

Having successfully incorporated a new rain scheme into ROMS that considers the mass contribution of rainfall, its effect is shown in several cases. This new rain scheme does not interfere with the existing temperature and salinity treatment of rainfall in ROMS. The added rain mass generated surface waves that increase in propagation speed with increasing depth. An error in the existing implementation of rain stress in ROMS produced a systematic overestimation of 41% in magnitude and up to 45° in direction. This error has been corrected in this study and its isolated effect on SSH in a tropical cyclone case is shown in an idealized set-up. Finally, the effect of rain mass and rain stress in a real storm surge case (Cyclone Monica) is compared with the effect of winds and atmospheric pressure. In this case, the effect of wind and pressure generated a surge of up to 170.6 cm and 61.5 cm respectively. The effect of rain mass increases the SSH up to 6.4 cm in Buckingham Bay. The effect of rain mass has a stronger remote presence compared to the effect of pressure and rain stress. Especially in semi-enclosed areas, the effect of rain mass can substantially contribute to the storm surge even when the storm is relatively far from the coastline, and both the effect of pressure and rain stress are no longer significant. An area is subjected to high rain stress when intense winds coincide with heavy rain. Here, the effect of rain stress increases the SSH up to 7.5 cm, but the effect is generally smaller than the effect of rain mass along the coast. Many ocean models ignore the mass effect of rainfall and only incorporate the effect of wind, atmospheric pressure and rain stress. However, this study shows that the effect of rain mass can be larger than the effect of pressure and rain stress in certain scenarios, and should not be neglected. Each process shows different spatial influence and cannot be accounted for by simply scaling up a certain effect, for example, recalibrating the surge model by scaling the wind field.

References

Bleck, R., & Boudra, D. B. (1981). Initial Testing of a Numerical Ocean Circulation Model Using a Hybrid (Quasi-Isopycnic) Vertical Coordinate. *Journal of Physical Oceanography, 11*(6), 755-770. doi: Doi 10.1175/1520-0485(1981)011<0755:Itoano>2.0.Co;2

Caldwell, D. R., & Elliott, W. P. (1970). Surface stresses produced by rainfall. *J. Phys. Oceanography, 1*, 145-148.

Chapman, D. C. (1985). Numerical treatment of cross-shelf open boundaries in a barotropic coastal ocean model. *Journal of Physical Oceanography, 15*(8), 1060-1075. doi: 10.1175/1520-0485(1985)015<1060:ntocso>2.0.co;2

Chen, C. S., Qi, J. H., Li, C. Y., Beardsley, R. C., Lin, H. C., Walker, R., & Gates, K. (2008). Complexity of the flooding/drying process in an estuarine tidal-creek salt-marsh system: An application of FVCOM. *Journal of Geophysical Research-Oceans, 113*(C7). doi: Artn C07052 Doi 10.1029/2007jc004328

Chou, M, & Suarez, and M. J. (1994). An efficient thermal infrared radiation parameterization for use in general circulation models. *NASA Tech. Memo., 104606*(3), 85pp.

Clayson, C. A., & Kantha, L. H. (1999). Turbulent kinetic energy and its dissipation rate in the equatorial mixed layer. *Journal of Physical Oceanography, 29*(9), 2146-2166. doi: Doi 10.1175/1520-0485(1999)029<2146:Tkeaid>2.0.Co;2

Codiga, D.L. (2011). Unified Tidal Analysis and Prediction Using the UTide Matlab Functions. *Technical Report 2011-01 Graduate School of Oceanography, University of Rhode Island, Narragansett, RI. 59pp*

Dodla, V. B., Desamsetti, S., & Yerramilli, A. (2011). A Comparison of HWRF, ARW and NMM Models in Hurricane Katrina (2005) Simulation. *International Journal of Environmental Research and Public Health, 8*(6), 2447-2469. doi: DOI 10.3390/ijerph8062447

Dudhia, J. (1989). Numerical Study of Convection Observed during the Winter Monsoon Experiment Using a Mesoscale Two-Dimensional Model. *Journal of the Atmospheric Sciences, 46*(20), 3077-3107. doi: Doi 10.1175/1520-0469(1989)046<3077:Nsocod>2.0.Co;2

Dudhia, Jimy. (1996). A multi-layer soil temperature model for MM5. *Sixth PSU/NCAR Mesoscale Model Users' Workshop*.

Durden, S. L. (2010). Remote Sensing and Modeling of Cyclone Monica near Peak Intensity. *Atmosphere, 1*(1), 15-33. doi: Doi 10.3390/Atmos1010015

Egbert, G. D., Bennett, A. F., & Foreman, M. G. G. (1994). TOPEX/POSEIDON tides estimated using a global inverse model. *Journal of Geophysical Research-Oceans, 99*(C12), 24821-24852. doi: 10.1029/94jc01894

Fairall, C. W., Bradley, E. F., Rogers, D. P., Edson, J. B., & Young, G. S. (1996). Bulk parameterization of air-sea fluxes for Tropical Ocean Global Atmosphere Coupled Ocean Atmosphere Response Experiment. *Journal of Geophysical Research-Oceans, 101*(C2), 3747-3764. doi: Doi 10.1029/95jc03205

Flather, R. A. (1976). A tidal model of the northwest European continental shelf *Mémoires de la Société Royale de Sciences de Liege* (Vol. 6, pp. 141-164).

Gill, A. E., and P. P. Niiler (1973). The theory of the seasonal variability in the ocean, *Deep Sea Res.*, 20, 141-177

Griffies, S. M., & Hallberg, R. W. (2000). Biharmonic friction with a Smagorinsky-like viscosity for use in large-scale eddy-permitting ocean models. *Monthly Weather Review, 128*(8), 2935-2946.

Hirose, N., I. Fukumori, *and* R. M. Ponte (2001). A non-isostatic global sea level response to barometric pressure near 5 days, *Geophys. Res. Lett.,* 28, 2441–2444, *doi:*10.1029/2001GL012907.

Hong, S. Y., Noh, Y., & Dudhia, J. (2006). A new vertical diffusion package with an explicit treatment of entrainment processes. *Monthly Weather Review, 134*(9), 2318-2341. doi: Doi 10.1175/Mwr3199.1

Huffman, G. J., Adler, R. F., Bolvin, D. T., Gu, G. J., Nelkin, E. J., Bowman, K. P., . . . Wolff, D. B. (2007). The TRMM multisatellite precipitation analysis (TMPA): Quasi-global, multiyear, combined-sensor precipitation estimates at fine scales. *Journal of Hydrometeorology, 8*(1), 38-55. doi: Doi 10.1175/Jhm560.1

Janjic, Z. I. (1994). The Step-Mountain Eta Coordinate Model - Further Developments of the Convection, Viscous Sublayer, and Turbulence Closure Schemes. *Monthly Weather Review, 122*(5), 927-945. doi: Doi 10.1175/1520-0493(1994)122<0927:Tsmecm>2.0.Co;2

Jarvinen, B. R., & Lawrence, M. B. (1985). An Evaluation of the Slosh Storm-Surge Model. *Bulletin of the American Meteorological Society, 66*(11), 1408-1411.

Kain, J. S. (2004). The Kain-Fritsch convective parameterization: An update. *Journal of Applied Meteorology, 43*(1), 170-181. doi: Doi 10.1175/1520-0450(2004)043<0170:Tkcpau>2.0.Co;2

Lin, Y. L., Farley, R. D., & Orville, H. D. (1983). Bulk Parameterization of the Snow Field in a Cloud Model. *Journal of Climate and Applied Meteorology, 22*(6), 1065-1092. doi: Doi 10.1175/1520-0450(1983)022<1065:Bpotsf>2.0.Co;2

Machta, L. (1969). Evaporation rates based on tritium measurements for hurricane Betsy. *Tellus*, *21*(3), 404-408.

Marchesiello, P., McWilliams, J. C. , & Shchepetkin, A. F. . (2001). Open boundary conditions for long-term integration of regional ocean models. *Ocean Modelling, 3*, 1-20.

Mlawer, E. J., Taubman, S. J., Brown, P. D., Iacono, M. J., & Clough, S. A. (1997). Radiative transfer for inhomogeneous atmospheres: RRTM, a validated correlated-k model for the longwave. *Journal of Geophysical Research-Atmospheres, 102*(D14), 16663-16682. doi: Doi 10.1029/97jd00237

Paulson, C. A. (1970). The mathematical representation of wind speed and temperature profiles in the unstable atmospheric surface layer. *J. Appl. Meteor., 9*, 857–861.

Peng, M. C., Xie, L., & Pietrafesa, L. J. (2004). A numerical study of storm surge and inundation in the Croatan-Albemarle-Pamlico Estuary System. *Estuarine Coastal and Shelf Science, 59*(1), 121-137. doi: DOI 10.1016/j.ecss.2003.07.010

Pickard, G. L., & Emery, W. J. (1990). *Descriptive physical oceanography: an introduction*. Elsevier.

Ponte, R. M. (2006). Oceanic response to surface loading effects neglected in volume-conserving models. *Journal of Physical Oceanography, 36*(3), 426-434. doi: 10.1175/Jpo2843.1

Rego, J. L., & Li, C. Y. (2010). Storm surge propagation in Galveston Bay during Hurricane Ike. *Journal of Marine Systems, 82*(4), 265-279. doi: DOI 10.1016/j.jmarsys.2010.06.001

Riehl H, Malkus J. (2011). Some aspects of hurricane Daisy, 1958. *Tellus A* 13(2)

Roden, G. I., & Rossby, H. T. (1999). Early Swedish contribution to oceanography: Nils Gissler (1715-71) and the inverted barometer effect. *Bulletin of the American Meteorological Society, 80*(4), 675-682. doi: Doi 10.1175/1520-0477(1999)080<0675:Escton>2.0.Co;2

Rogers, Eric, , Thomas Black, , Brad Ferrier, , Ying Lin, , David Parrish, & , and Geoffrey DiMego. (2001). National Oceanic and Atmospheric Administration Changes to the NCEP Meso Eta Analysis and Forecast System: Increase in resolution, new cloud microphysics, modified precipitation assimilation, modified 3DVAR analysis. *NOAA*.

Saha, S., Moorthi, S., Pan, H. L., Wu, X. R., Wang, J. D., Nadiga, S., Goldberg, M. (2010). The Ncep Climate Forecast System Reanalysis. *Bulletin of the American Meteorological Society, 91*(8), 1015-1057. doi: Doi 10.1175/2010bams3001.1

Shchepetkin, A. F., & McWilliams, J. C. (2005). The regional oceanic modeling system (ROMS): a split-explicit, free-surface, topography-following-coordinate oceanic model. *Ocean Modelling, 9*(4), 347-404. doi: DOI 10.1016/j.ocemod.2004.08.002

Sheng, Y. P., Alymov, V., & Paramygin, V. A. (2010). Simulation of storm surge, wave, currents, and inundation in the Outer Banks and Chesapeake Bay during Hurricane Isabel in 2003: The importance of waves. *Journal of Geophysical Research-Oceans, 115*. doi: Artn C04008 Doi 10.1029/2009jc005402

Sheng, Y. P., Davis, J. R., Figueiredo, R., Liu, B., Liu, H., Luettich, R., Zheng, L. (2012). A regional testbed for storm surge and coastal inundation models - an overview. *Estuarine and Coastal Modeling, American Society of Civil Engineers*, 476-495.

Skamarock, W. C, Klemp, J. B, Dudhia, J, Gill, D. O, Baker, D. M, Duda, M. G, JG., Power. (2008). A Description of the Advanced Research WRF Version 3. . *NCAR/TN-475+STR*.

Smith, W. H. F., and Sandwell D. T. . (1997). Global seafloor topography from satellite altimetry and ship depth soundings. *Science, 277*, 1957-1962.

Stewart, Robert H. (2009). Introduction to Physical Oceanography. *University Press of Florida*.

Umlauf, L., & Burchard, H. (2003). A generic length-scale equation for geophysical turbulence models. *Journal of Marine Research, 61*(2), 235-265. doi: 10.1357/002224003322005087

Van Dorn, W. G. (1953). Wind stress on an artificial pond. *Journal of marine research, 12*, 249-276.

Wang, Shuai, Toumi, Ralf, Czaja, Arnaud, & Van Kan, Adrian. (2015). An Analytic Model of Tropical Cyclone Wind Profiles. *Quarterly Journal of the Royal Meteorological Society*, n/a-n/a. doi: 10.1002/qj.2586

Watson, P. J. (2011). Is There Evidence Yet of Acceleration in Mean Sea Level Rise around Mainland Australia? *Journal of Coastal Research, 27*(2), 368-377. doi: Doi 10.2112/Jcoastres-D-10-00141.1

Weisberg, R. H., & Zheng, L. Y. (2006). Hurricane storm surge simulations for Tampa Bay. *Estuaries and Coasts, 29*(6A), 899-913.

Westerink, J. J., Luettich, R. A., Baptista, A. M., Scheffner, N. W., & Farrar, P. (1992). Tide and Storm-Surge Predictions Using Finite-Element Model. *Journal of Hydraulic Engineering-Asce, 118*(10), 1373-1390. doi: Doi 10.1061/(Asce)0733-9429(1992)118:10(1373)

Westerink, J. J., Luettich, R. A., Feyen, J. C., Atkinson, J. H., Dawson, C., Roberts, H. J., Pourtaheri, H. (2008). A basin- to channel-scale unstructured grid hurricane storm surge model applied to southern Louisiana. *Monthly Weather Review, 136*(3), 833-864. doi: Doi 10.1175/2007mwr1946.1

Wu, C. C. (2013). TYPHOON MORAKOT Key Findings from the Journal TAO for Improving Prediction of Extreme Rains at Landfall. *Bulletin of the American Meteorological Society, 94*(2), 155-160. doi: Doi 10.1175/Bams-D-11-00155.1

Zhong, L. J., Li, M., & Zhang, D. L. (2010). How do uncertainties in hurricane model forecasts affect storm surge predictions in a semi-enclosed bay? *Estuarine Coastal and Shelf Science, 90*(2), 61-72. doi: DOI 10.1016/j.ecss.2010.07.001

Effect of extreme ocean precipitation on sea surface elevation and storm surges

Running head: Effect of extreme rainfall on sea surface elevation and storm surges

Benjamin Wong (corresponding author): benjamin.wong11@imperial.ac.uk

Ralf Toumi: r.toumi@imperial.ac.uk

Space and Atmospheric Physics Group,

Blackett Laboratory,

Imperial College London,

London SW7 2AZ,

UK

Keywords: ocean modelling, Cyclone Monica, rain mass, rain stress

Abstract

Ocean models that neglect mass and momentum contributions from precipitation can have a systematic bias in sea surface height (SSH). Here, a new rainfall scheme is introduced into the Regional Ocean Modelling System (ROMS) to incorporate the effects of precipitation mass. When precipitation is added to the sea surface, it spreads out via surface gravity waves that increase in propagation speed with increasing water depth. Over several days, the SSH increase due to the precipitation mass added created a geostrophic adjustment, generating anti-cyclonic geostrophic currents around the SSH increase. The transfer of momentum from precipitation to the sea surface, or rain stress, can also be important. In the case study of a real tropical cyclone, Monica passing North Australia, the effect of incorporating precipitation mass is compared with other processes affecting the storm surge: surface wind, inverse barometer effect and rain stress. The maximum SSH response is 170.6 cm for the wind effect, 61.5 cm for the inverse barometer effect, 7.5 cm for the effect of rain stress and 6.4 cm for the effect of rain mass. Each process has been shown to have different spatial influences. The effect of rain mass has a strong remote influence compared to the inverse barometer effect and the effect of rain stress. This is particularly seen in semi-enclosed bays.

1 Introduction

The contribution of oceanic precipitation to storm surges has so far been neglected in storm surge models, typically only incorporating the contributions of the inverse barometer effect (Roden et al., 1999) and wind driven effect towards the overall surge height. There is very little work addressing the contribution of oceanic precipitation to surge levels. This is expected, considering that many ocean models do not incorporate the mass and momentum effect of precipitation for it to be studied in detail. Sheng et al. (2012) described a test platform used to review several established storm surge models such as CH3D-SSMS (Sheng et al., 2010), ADCIRC (Westerink et al., 1992), FVCOM (Chen et al., 2008), CMEPS (Peng et al., 2004) and SLOSH (Jarvinen et al., 1985). Thirty scenarios were used to test their sensitivity towards parameters such as bathymetry, storm forcing, wind drag coefficient, bottom friction, Coriolis and 2D-3D formulation, but precipitation was not investigated. Ocean models such as ROMS (Shchepetkin et al., 2005) and FVCOM only incorporate the effect of temperature, salinity and momentum from rain, but not the effect of rain mass. Storm surge models such as ADCIRC and SLOSH ignore the effects of ocean rain entirely. Ponte (2006) incorporated realistic freshwater fluxes in a global barotropic model and found that they can cause annual standard deviations in sea surface level as large as 1 cm, especially in shallow and semi-enclosed regions. In highly precipitating storm events with extreme rain rates, the sea surface height increase may be more substantial. For instance, the highest rainfall recorded by Typhoon Morakot in 2009 was up to 74 cm day^{-1} (Wu, 2013). How this contributes to storm surges and to what extent rain mass can be neglected in this case is not known.

Here, a new rainfall scheme has been introduced into ROMS to account for the effect of rain mass. This scheme complements the existing rainfall routine in ROMS where only temperature and salinity changes due to rainfall are accounted for. An idealized set-up of ROMS will be used to isolate the effects of adding rain mass to the sea surface height. The Weather Research and Forecasting model (WRF, Skamarock et al., 2008) is used to generate the rain forcing to evaluate the sea surface height response in ROMS.

The transfer of momentum from raindrops to the water surface, or rain stress, was first documented by Van Dorn (1953), who concluded that the stress contributions from rainfall can considerably intensify surface stresses. Caldwell et al. (1970) have since built on his work, parameterizing rain stress as a function of rain rate and wind speed. This parameterization has been widely incorporated in many model studies such as the one-dimensional mixed layer model developed by Clayson et al. (1999) and the bulk parameterization outlined by Fairall et al. (1996) relating the near-surface atmospheric and the oceanographic bulk variables. This air-sea bulk parameterization has also been adopted in ROMS. While the parameterization of rain stress has been widely incorporated, there has been no study so far that shows its isolated effect in the models it has been implemented in. For the case of tropical cyclones, where extreme wind speeds and precipitation rates are found, the isolated effect of rain stress has not been shown and its contribution to storm surges is not known. This section shall employ the use of an idealised set-up in ROMS to show the isolated effects of rain stress in the context of storm surges.

Finally, a real case scenario is studied to compare the various processes affecting storm surges. Tropical Cyclone Monica (Durden, 2010) has been chosen for her high wind speed, low system pressure and high rainfall, which are the key storm surge effects investigated here. A validated atmospheric state is generated using WRF and is prescribed onto ROMS to investigate how various processes affect the storm surge. The significance of rain mass and rain stress is compared with two other established storm surge processes: the inverse barometer effect and the effect of surface wind. Each of these physical effects is investigated based on their isolated contribution to the total SSH and storm surge patterns.

2 Model set-up and validation

2.1 Set-up of idealized case

Rain mass is introduced to ROMS through a new rainfall scheme that incorporates rain rate as point sources. This approach is similar to how river run-off is introduced to the model, but in this case, vertical fluxes are added instead of horizontal fluxes. The rainfall rate from the atmospheric rain forcing is converted into point sources without further prescribing its temperature and salinity. The temperature and salinity of rain is accounted for within the existing bulk flux routine where air-sea momentum and energy exchanges are calculated (Fairall et al., 1996). An idealized set-up of ROMS is used to create a controlled environment, isolating the specific effects investigated here. The ROMS grid is set up with closed boundaries, a horizontal resolution of 15 km, 21 vertical levels and a spatial extent 5°N to 35°N and 120°E to 180°E. The initial ocean state has a uniform temperature of 26°C and salinity of 35 psu. The land mask is specified at the western boundary up to 140°E to simulate the coastline. A third-order upwind scheme is used for horizontal momentum advection, and a Smagorinsky-like viscosity is applied (Griffies et al., 2000). The turbulence closure scheme used to calculate vertical mixing is based on the Generic Length Scale (GLS) parameterization as described by Umlauf et al. (2003).

An idealized tropical cyclone is simulated using WRF and prescribed onto ROMS. The set-up of the initial cyclone profile and atmospheric state follows Wang et al. (2015). For the WRF simulation, one single nest is set up with 31 vertical levels and a horizontal resolution of 15 km in the domain spanning 5°N to 35°N and 120°E to 180°E. The microphysical parameterization used is based on Lin et al. (1983). Cumulus parameterization is not included, which reduces the computational time required for each simulation. Without cumulus parameterization, the amount of precipitation may be underestimated at a 15 km horizontal resolution. However, the aim of this part of the study is to understand the specific effect of adding precipitation mass to the ocean model in a simple, idealized set-up, and not to reproduce the atmospheric domain with high accuracy. The surface layer scheme is based on Monin-Obukhov, with Zilitinkevich thermal roughness length and standard similarity functions (Paulson, 1970). Planetary boundary layer processes are parameterized using the Mellor-Yamada-Janjic scheme (Janjic, 1994). The longwave and shortwave radiation schemes are implemented from Mlawer et al. (1997) and J. Dudhia (1989) respectively.

2.2 Rain stress parameterization

In ROMS, rain stress is implemented in the bulk fluxes routine from Fairall et al. (1996) and based on the parameterization by Caldwell and Elliott (1970) as follows:

$$\tau_{rx} = 0.85 R \rho_r |\vec{v}_{10}| * SIGN(U_{10}) \quad (1)$$

$$\tau_{ry} = 0.85 R \rho_r |\vec{v}_{10}| * SIGN(V_{10}) \quad (2)$$

where R is the rain rate, ρ_r is the density of rainwater, τ_{rx} is the rain stress in the x direction, $SIGN(U_{10})$ denotes the sign of U_{10} (U-component wind speed at 10 m), τ_{ry} is the rain stress in the y direction and $SIGN(V_{10})$ denotes the sign of V_{10} (V-component wind speed at 10 m).

The rain stress parameterization of Caldwell and Elliott (1970) is derived from a one-dimensional model where $\vec{v}_{10}$ refers to the wind velocity in the direction of reference. When considering wind velocity resolved into its orthogonal components, it would be incorrect to utilize the total velocity in calculating the rain stress. Here, the magnitude of the u-component winds (U) and the v-component winds (V) used in the calculation of rain stress will always be $\sqrt{U^2+V^2}$. This results in a systematic overestimation in the magnitude of rain stress by a factor of $\sqrt{2}$. The error in the direction of rain stress is more inconsistent. Since U and V are always set to be equal in magnitude (equal to the net wind speed), the directions of the rain stress can only be in any of the four directions: 45°, 135°, 225° and 315°, unless there is zero rainfall or zero wind speed. Furthermore, the existing ROMS rain stress code always assigns a positive sign to zero values. For example, if U is zero, it will still be assigned the magnitude of V (now equal to the magnitude of the net wind speed), with the direction of positive U. The error in the direction of the rain stress term can range from 0° (when U=V) to 45° (when either U=0 or V=0). Overall, this results in a systematic overestimation of rain stress and an incorrect direction calculated for the overall wind stress.

The corrected implementation of the rain stress parameterization is as follows:

$$\tau_{rx} = 0.85R\rho_r U_{10} \tag{3}$$

$$\tau_{ry} = 0.85R\rho_r V_{10} \tag{4}$$

An idealized set-up of ROMS is used to verify the corrected implementation of rain stress. Here, the u-component wind is set to a constant -1 m s^{-1} and the v-component wind is set to zero. One centimetre of rain is introduced to a single cell (15 km by 15 km) in the centre of the domain (20°N 150°E) at the first hour. Two simulation runs are conducted to compare the existing implementation of rain stress (using equations (1) and (2)) with the corrected implementation of rain stress (using equations (3) and (4)). Both simulation runs are subtracted from a control run without any rain stress to eliminate any noise such as the SSH response to the background u-component wind.

2.3 Set-up of real case

The ROMS set-up uses a single grid at a horizontal resolution of 6 km, with the open boundaries using the Flather (1976) conditions for the barotropic velocities and the Chapman (1985) conditions for sea surface elevation. A minimum depth of 10 m and maximum depth of 5500 m has been specified. Twenty layers are chosen in the vertically stretched terrain-following sigma-coordinate, with higher resolution placed at the surface and lower resolution placed at the bottom. Geometry of the bathymetry is obtained from Global Topography v14.1 (Smith, 1997). The tidal forcing is applied at the open boundaries and imposed on the elevation and the barotropic velocities. It is derived from 11 tidal harmonics that are extracted from the 1/12° resolution Pacific Ocean Atlas solution provided by the Oregon State University (OSU) Tidal Data Inversion (Egbert et al., 1994). A nudging relaxation zone with eight grids from the boundary is set up to relax the baroclinic structure to the forcing fields at the boundary (Marchesiello et al., 2001). The 1/12° resolution HYbrid Coordinate Ocean Model (HYCOM) (Bleck et al., 1981) global daily analysis data is used as the initial, boundary and nudging conditions for the model.

The pressure-driven effect in ROMS is obtained by applying the atmospheric pressure field from WRF and the sea level is adjusted based on the inverse barometer approximation (Gill and Niiler, 1973). The inverse barometer effect is generally a good approximation for sea level responses to local atmospheric pressure. For non-isostatic pressure effects, Hirose et al. (2001) found that deviations from the inverse barometer effect contributed only up to 2 cm in large-scale basins such as the Pacific and Atlantic Ocean. For smaller-scale basins such as Cape of Carpentaria, the non-isostatic deviation was under 0.5 cm and is much smaller compared to the precipitation effects in this case (Figure 10b).

WRF is used to simulate a high resolution atmospheric state of tropical cyclone Monica to be prescribed onto the ocean model for the case study. Two nests are employed with 28 vertical levels. The final grid has a horizontal resolution of 6 km. NCEP Climate Forecast System Reanalysis (CFSR) (Saha et al., 2010) has been used for initial and lateral boundary conditions. The boundary forcing is prescribed every 6 hours and the model interior is allowed to evolve freely. The ETA scheme (Rogers et al., 2001) is chosen for microphysical parameterization. The Kain-Fritsch cumulus parameterization scheme (Kain, 2004) has been used for both nests. The surface layer scheme is based on Monin-Obukhov with Carslon-Boland viscous sub-layer and standard similarity functions. The selected planetary boundary layer is from Yonsei University (Hong et al., 2006). The Mesoscale Model 5 (MM5) 5-layer thermal soil temperature model (Dudhia, 1996) is used to calculate the heat and moisture fluxes over the land. The longwave and shortwave radiation schemes are implemented from Mlawer et al. (1997) and Chou et al. (1994) respectively.

The isolated effects of including precipitation mass source, rain stress, inverse barometer effect and surface wind forcing are individually investigated by comparing with four separate configurations that are simulated with precipitation mass source, without rain stress, without the inverse barometer correction and without surface wind forcing respectively. The five experiments conducted are tabulated in Table 2.1. Spatial plots of SSH are differenced from the control simulation (Case A) to illustrate the isolated effects of each process.

Cases	*WRF wind conditions applied to ROMS*	*Inverse barometer effect in ROMS*	*Rain stress effect in ROMS*	*New rain mass scheme*
Case A	Wind forcing applied	Turned ON	Turned ON	NOT used
Case B	NO wind forcing applied	Turned ON	Turned ON	NOT used
Case C	Wind forcing applied	Turned OFF	Turned ON	NOT used
Case D	Wind forcing applied	Turned ON	Turned OFF	NOT used
Case E	Wind forcing applied	Turned ON	Turned ON	In use

Table 2.1: Cases set up with different ROMS model options and wind conditions.

3 Results

3.1 Idealized case: response to rain mass

An idealized set-up of ROMS is used to study the effect of rainfall mass on sea surface elevation. The effect of rainfall is isolated by setting the wind field to zero and all other atmospheric forcings are set to a constant nominal value. Rain is introduced to a single grid cell (15 km by 15 km) at 20°N 150°E for 1 hour at the rate of 1 cm/h, to understand the effect of a single-point perturbation on the free surface. Figure 1 shows the ocean surface response after 2 hours and 9 hours. The illustrations are zoomed into the area 9°N to 31°N and 134°E to 176°E. A surface gravity wave is generated, propagating radially outwards from the point of perturbation. At time = 1 h, the maximum SSH is 0.0181 cm and the minimum is -0.0076 cm. At time = 9 h, the maximum SSH is 0.0043 cm, the minimum is -0.0045 cm and the wave propagates to about 10° from the initial point of perturbation. Over 9 hours, the amplitude of the gravity wave drops by about 76%.

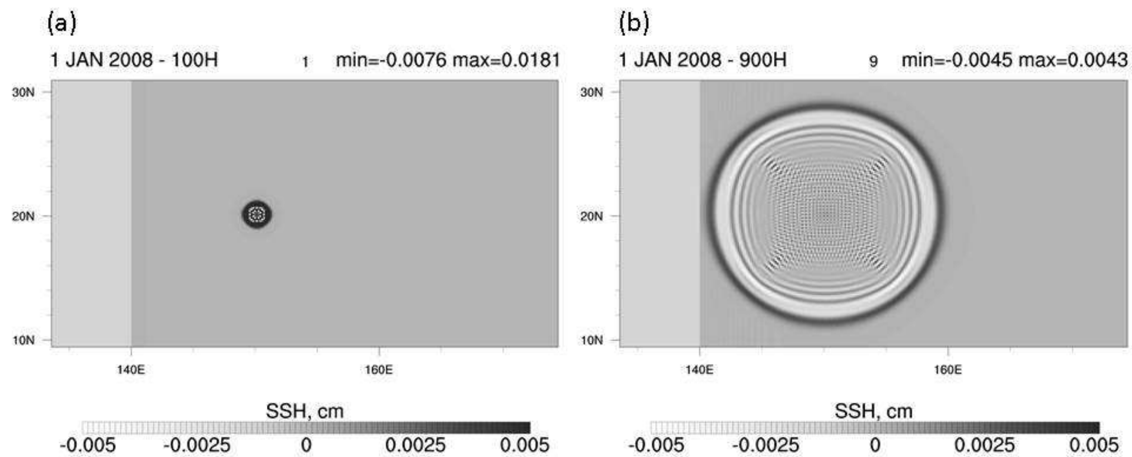

Figure 1: SSH response to rain mass addition to a single surface grid cell after (a) 1 hour and (b) 9 hours. Land is west of 140°E, ocean is east of 140°E. Wind forcing is set to zero.

Next, the SSH response to rainfall at a longer time scale is studied by forcing ROMS with rainfall from an idealized tropical cyclone simulated using WRF over 8 days. The maximum rain rate is not at the centre of the cyclone, but along the rain bands. As the cyclone treks from the east to the west of the domain, it gradually grows in size and intensity. The rain bands of the tropical cyclone also increase in size with time. Figure 2 shows the cumulative rainfall throughout the event, with a maximum of 319 mm at any one grid. To avoid any interference from the winds, the wind field is set to zero so the sea surface is unaffected by wind stress and responds only to the cyclone rainfall.

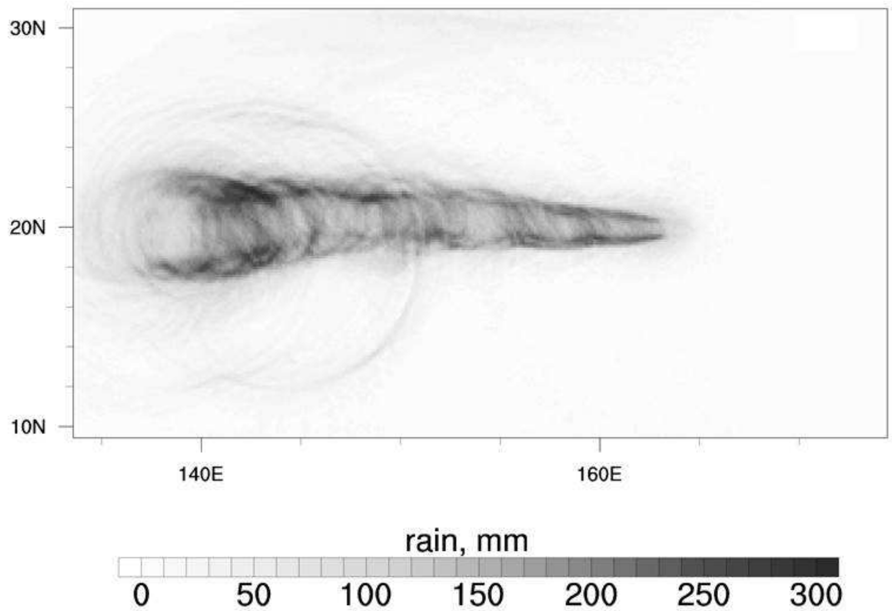

Figure 2: Cumulative rainfall of the idealized tropical cyclone over 8 days.

The SSH response to rainfall from the idealized tropical cyclone is simulated for two ocean depths at 100 m and 1000 m deep. Figure 3 shows the SSH at the 170th hour of the simulation when the tropical cyclone makes landfall at the coastline along 140°E. For both depths, the SSH increases along the rainfall path and gradually decreases towards the domain boundaries. For the case with a depth of 100 m, the maximum SSH is 5.8 cm and the minimum SSH is 1.3 cm at the 170th hour. A clockwise gyre is formed, with the sea surface currents at a magnitude of 10^{-2} m s^{-1}. For the case with a depth of 1000 m, the maximum SSH is 3.2 cm while the minimum SSH is 2.3 cm. A weaker clockwise gyre is formed with the sea surface currents at a magnitude of 10^{-3} m s^{-1}.

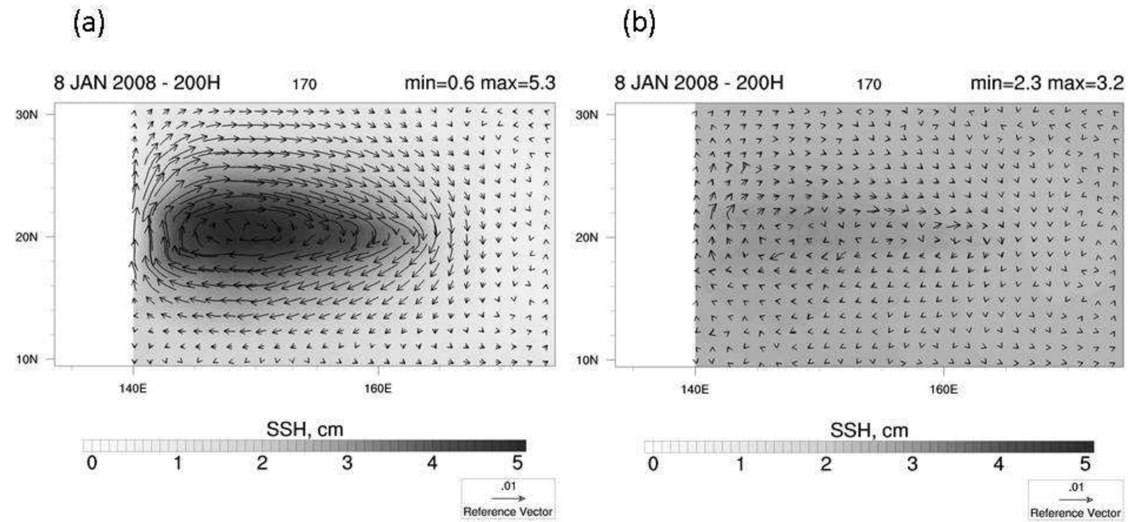

Figure 3: SSH and sea surface current response to the rain mass added to the ocean with (a) 100 m depth and (b) 1000 m depth at the 170th hour.

3.2 Idealized case: response to rain stress

Figure 4 shows the rain stress perturbation setting off a surface gravity wave that propagates outwards from the point of perturbation towards the domain boundaries. Two implementations are shown for the existing and the corrected model. In the existing implementation of rain stress (Figure 4a), the resulting surface gravity wave is at an angle of 45° to the wind direction. The front of the wave is led by a crest in the north-westward direction with an amplitude of up to 0.01 cm. In the south-eastward direction, the wave is led by a trough of up to 0.01 cm in amplitude. Figure 4b shows the SSH response to the corrected implementation of rain stress in ROMS. The surface gravity wave generated from the rain stress perturbation is now symmetrical to the wind direction. In the westward direction, the front of the wave is led by a crest of up to 0.005 cm in amplitude. In the eastward direction, the wave is led by a trough of up to 0.005 cm in amplitude.

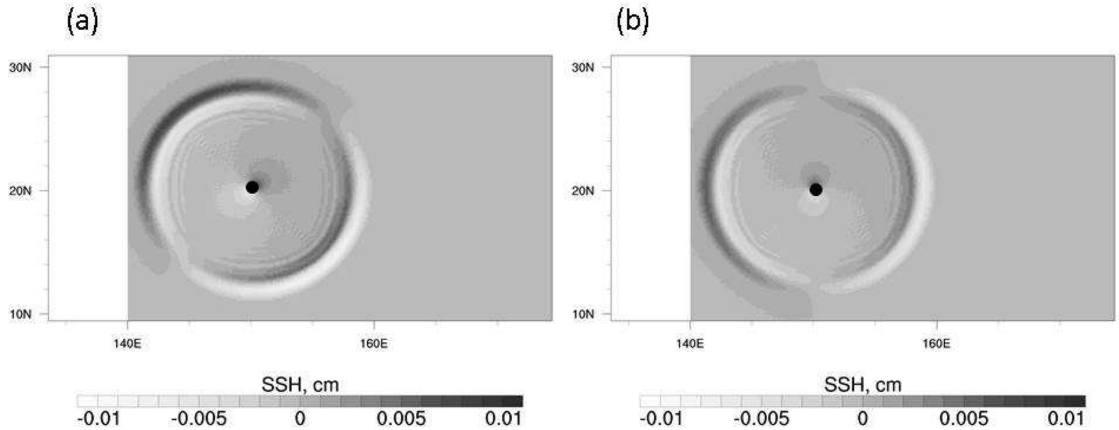

Figure 4: Sea surface height at 10 hours after introducing a rain stress perturbation for (a) the existing implementation of rain stress in ROMS and (b) the corrected implementation of rain stress in ROMS. The black dot in the centre of the domain (20°N 150°E) denotes the initial position of perturbation. Wind forcing is set to zero.

Next, the contribution of rain stress to storm surges is investigated by forcing ROMS with an idealized tropical cyclone simulated using WRF. Here, the wind and rainfall fields are retained, but the other forcing fields are set to a nominal and constant value in order not to introduce interfering signals into the system. To show the isolated effect of rain stress, the response of SSH and sea surface currents from the rain stress simulation was subtracted from a control simulation (Figure 5). Here, an anticlockwise circulation centering 20°N 141°E is generated with a decrease in SSH at the circulation centre. The positive surge is up to +0.44 cm and the negative surge is up to -0.63 cm.

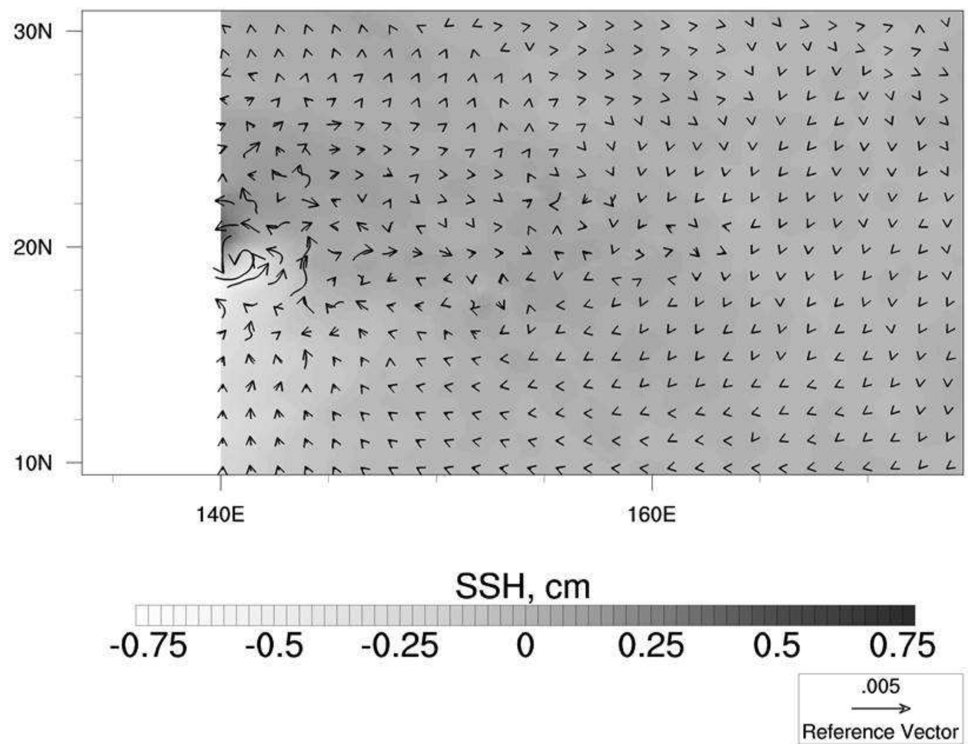

Figure 5: Response of SSH and sea surface currents to rain stress at t = 163 h.

3.3 Case study: validation of Cyclone Monica

The atmospheric state is simulated for the period between 20 April 2006 and 24 April 2006. Minimum sea level pressure from WRF is used to generate the cyclone path for comparison as shown in Figure 6. This cyclone path is validated using the storm track provided by the Australian Bureau of Meteorology (BOM, http://www.bom.gov.au/cyclone). On 20 April 2006, both the modelled cyclone and the observed cyclone are located at the western coast of Cape York Peninsula, but the modelled cyclone is situated more northwards compared to the observed cyclone. The modelled path is largely similar to the observed path, but has a northward offset of up to 1°. The modelled cyclone also travels faster than the observed cyclone by up to a day.

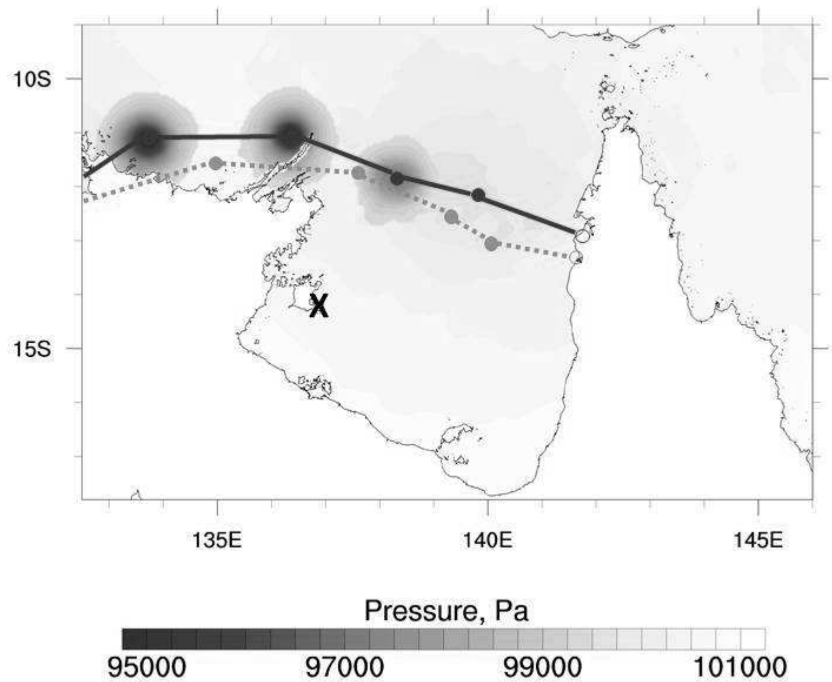

Figure 6: Cyclone path of WRF (solid line) and observations from BOM cyclone report (dashed line). Filled circles are positions every 24 hours from 0000 UTC 20 April 2006 (open circle). Location of the Groote Elyandt weather station is indicated with an 'X'.

Based on the observed weather conditions provided by BOM, the maximum wind speed observed at Cape Wessel (11°S, 136.8°E) and Maningrida (12°S, 134.2°E) were 130 km h^{-1} and 148 km h^{-1} respectively. In WRF, the maximum modelled wind speed at Cape Wessel and Maningrida were 141 km h^{-1} and 146 km h^{-1} respectively, which compared well with observations (Figure 7).

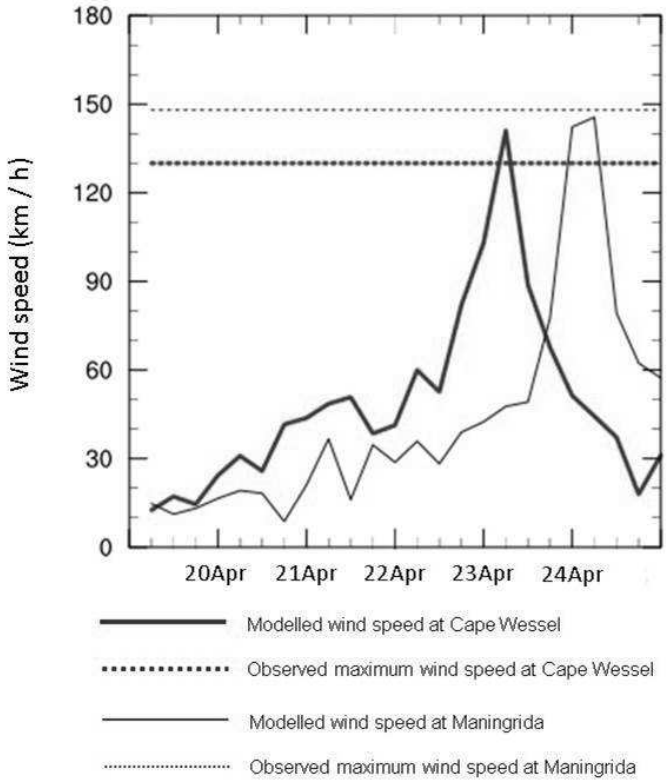

Figure 7: Comparison of the modelled wind speeds at Cape Wessel (11°S, 136.8°E) and Maningrida (12°S, 134.2°E) with the maximum wind speeds observed.

The simulated precipitation is compared with the multi-satellite rainfall estimates from the Tropical Rainfall Measuring Mission (TRMM) 3B42 version 6 (Huffman et al., 2007) (Figure 8). The modelled rainfall path is largely in line with the observed rainfall path but the rainfall is more intense along the cyclone track and less intense away from the track. The observed cumulative rainfall (TRMM) is more homogeneous, having more regions with 100 – 300 mm of rainfall. Nevertheless, the domain cumulative rainfall in WRF is 6% more than that observed by TRMM, although this percentage is expected to be higher since the WRF rainfall is summed with the land mask applied, while TRMM rainfall is summed over every cell in the domain. The total domain cumulative rainfall simulated using WRF is 4.7×10^6 mm and the observed cumulative rainfall in TRMM is 4.4 x 10^6 mm over 8 days. However, this is not a large concern in this case study since the main objectives are to simulate and compare various processes in a realistic environment and not to closely replicate the exact storm event. The precipitation rates modelled here are not uncommon among tropical cyclones in Australia and similar storm systems in other parts of the world. From the BOM reports on historical tropical cyclones, the highest observed precipitation rates of Monica was 340 mm day^{-1}, Laurence (December 2009) at 402 mm day^{-1}, Paul (March 2010) at 443 mm day^{-1} and Yasi (January 2011) at 471 mm day^{-1}. Outside of Australia, the estimated maximum rainfall of Hurricane Katrina (August 2005) was 300 mm day^{-1} (Dodla et al., 2011) and Typhoon Morakot (August 2009) was 741 mm day^{-1} (Wu, 2013). Hence, the rainfall produced by Monica is not an extreme case compared to other tropical cyclones and the overestimation in the rainfall simulated here does not lead to an unrealistic scenario.

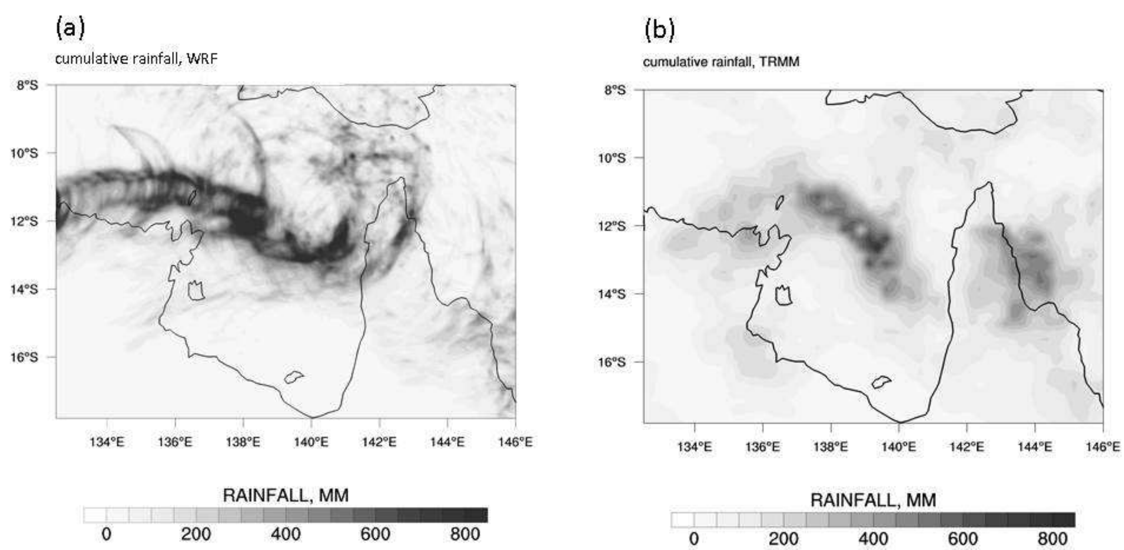

Figure 8: 8-Day cumulative rainfall output from 19 April 2006 for (a) WRF and (b) TRMM.

The configuration of ROMS used for validating the ocean state incorporated the effects of rain mass, rain stress, the inverse barometer effect and all atmospheric forcings including wind. The storm surge (Figure 9) is validated against the tidal gauge measurements taken from Milner Bay in Groote Elyandt. The tidal gauge data is obtained from the Australian Baseline Sea Level Monitoring Project (ABSLMP) (Watson, 2011). To compare the storm surge, the tidal components are detided using the tidal package by Codiga (2011). The tidal range is very large and there remains a residual tidal-like signal after de-tiding eleven tidal components that were introduced into ROMS in the tidal forcing set-up. At this location, the surge simulated in ROMS (23 April 2006) is earlier than the observed data (24 April 2006) by a day. However, the magnitude of the surge is very well-captured. The difference in modelled and observed time of peak surge is also consistent with the different translation speed and track of the WRF cyclone. The modelled cyclone is located north of the Groote Elyandt station around 1200 UTC 22 April 2006, while the observed cyclone reaches north of the Groote Elyandt station around 0000 UTC 24 April 2006. However, the modelled cyclone path is situated more north compared to the observed cyclone path and a longer time is expected for the storm surge to be picked up at Groote Elyandt. Hence, an overall difference of a day can be expected between the modelled and observed storm surge.

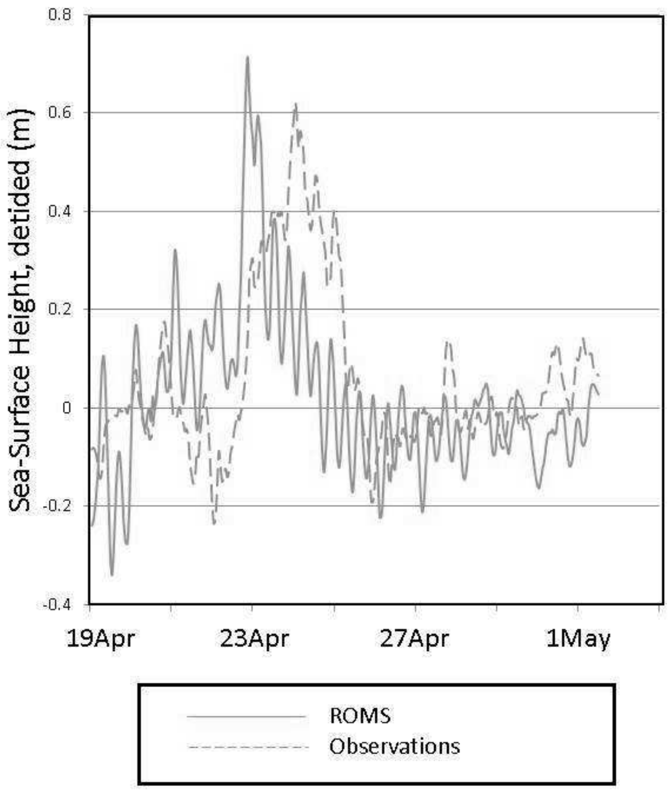

Figure 9: Comparison between the storm surge generated in ROMS with tidal gauge measurements (detided) at Groote Elyandt weather station obtained from ABSLMP, with the location indicated with an 'X' on Figure 6.

3.4 Case study: contribution of rain to SSH

We examine the individual contributions to the SSH response to Cyclone Monica. The SSH response to the effect of wind (Figure 10a) is the largest compared to the other effects. On 21 April 2006, the negative surge is up to -58 cm at the south-eastern boundary of the Gulf of Carpentaria and the positive surge is up to 61 cm on the western boundary. On 22 April 2006, the negative surge at the south-eastern boundary of the gulf and the positive surge at the western boundary still persist. There is a region of negative SSH located at the centre of the gulf. The minimum SSH is -57 cm and maximum SSH is 60 cm. On 23 April 2006, the cyclone reaches the Wessel Islands and the SSH rises up to 171 cm in Buckingham Bay (12°S 136°E). The positive surge at the western boundary of the gulf is still present at this time, but the negative surge at the south-eastern boundary has reverted to its nominal levels. At the northern coast of the Arnhem Land, the negative surge is up to -111 cm.

Figure 10b shows the SSH change due to the inverse barometer effect. The SSH increase is localized to the position of the cyclone and increases as the cyclone intensifies through the event. The distribution of the SSH scalar field is similar to atmospheric pressure, with the highest SSH at the centre of the cyclone, gradually decreasing with distance from the cyclone centre. The SSH increases from 13 cm on 21 April 2006 to 61.5 cm on 23 April 2006 as the cyclone intensifies.

The additional SSH response due to the effect of rain stress is shown in Figure 10c. On 21 April 2006, the additional negative surge is up to -2.4 cm on west coast of Cape York Peninsula. There is an additional positive SSH of up to 0.9 cm near the position of the cyclone centre. On 22 April 2006, when Monica is at the centre of the Gulf of Carpentaria, there is an additional positive SSH of up to 0.7 cm ahead of the cyclone and a negative SSH of up to -1.1 cm behind the cyclone. On 23 April 2006, there is an additional positive surge of up to 7.5 cm to the east of the Wessel islands and an additional negative surge of up to -2.9 cm to the west of the islands.

Figure 10d shows the additional SSH response due to rain mass, increasing as the cyclone tracks across the Gulf of Carpentaria and decreasing when the cyclone passes. On 21 April 2006, Monica is situated at the western coast of Cape York Peninsula and the SSH rises up to 3.7 cm at the coast. On 22 April 2006, Monica is centred in the gulf and the SSH increases up to 4.6 cm, spreading out to the rest of the gulf. The sea level at the southern boundary of the gulf increases up to 3.5 cm. On 23 April 2006, the cyclone reaches the Wessel Islands and the SSH rises up to an additional 6.4 cm. The sea level change at the southern boundary of the gulf decreases to 2 cm.

(a)

(b)

(c)

(d)

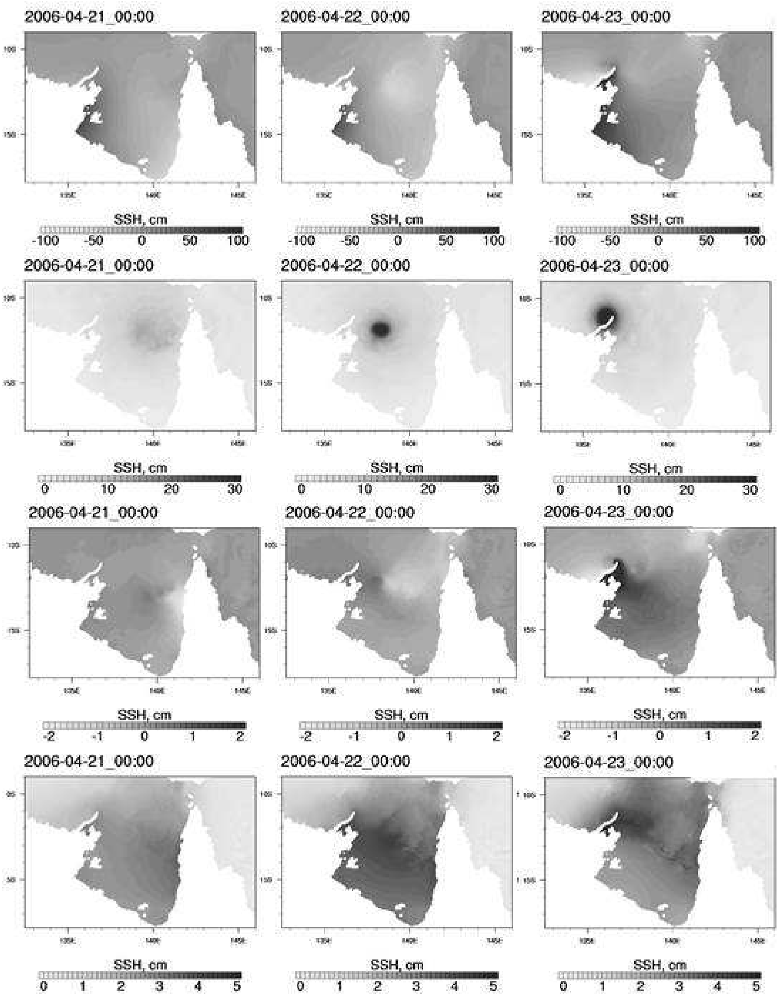

Figure 10: Additional SSH response to the effect of (a) wind, (b) atmospheric pressure, (c) rain stress and (d) rain mass from 21 April 2006 to 23 April 2006.

4 Discussion

The rain mass perturbation on the water surface sets off a surface gravity wave propagating outwards towards the domain boundaries over a time scale of several hours (Figure 1). Characteristics of surface waves are inherently non-linear. But considering shallow water approximations (Stewart, 2009), where the water depth is much smaller than the wavelength, the phase speed (c) can be expressed as:

$$c = \sqrt{gd} \tag{5}$$

where g is the gravitational acceleration and d is the depth of water.

From the initial point of perturbation, the surface wave propagated from 20°N 150°E to 20°N 160°E in 9 hours translating at a speed of 30.9 m s^{-1}. The shallow water approximation is valid for water depths much lesser than the wavelength. Here, the water depth is 100 m while the wavelength is about 100 km. The water depth in this case is only 0.1% that of the wavelength, making the shallow water approximation a valid assumption. From equation (5), the surface gravity wave in this case should advance at a phase speed of 31.3 m s^{-1}, which is consistent with the ROMS output.

Next, the SSH response at a longer time scale is examined using an idealized tropical cyclone to force the ocean model over 8 days. In Figure 3, the added mass spreads outwards from the mass sources towards the domain boundaries via gravity waves. In the deeper ocean case, the maximum SSH is smaller (up to 3.2 cm) compared to the shallow ocean case (up to 5.3 cm). From equation (5), gravity waves in the deeper case travel 3 times faster than in the shallow water case, which accounts for the faster decrease in the maximum SSH for the deeper ocean case. With the rain mass spreading out faster in the deeper ocean, the minimum SSH reaches a higher level for the deep ocean case (2.3 cm) compared to the shallow ocean case (1.3 cm). At longer time scales (after 7 days), a pressure gradient is generated from the sea surface height increase. This creates a geostrophic adjustment with an opposing Coriolis force. Geostrophic currents of the magnitude 0.01 m s^{-1} are generated, rotating in a clockwise direction.

With the implementation of rain stress now corrected in ROMS, the SSH response to rain stress is shown by forcing ROMS with an idealized tropical cyclone (Figure 5). Rain stress is parameterized as a function of rain rate and wind speed and follows the direction of the winds. Hence, rain stress is only exerted in areas where non-zero values of rain rate and wind speed coincide. In the case of a tropical cyclone, rainfall is highest along the rain bands towards the centre of the cyclone. Rain stress contributes to storm surges in a manner similar to wind stress. The anti-clockwise rotating rain stress creates an anti-clockwise gyre at the sea surface. Coriolis force deflects the currents to the right and generates an outward diverging flow that decreases the SSH at the centre of the gyre.

Finally, a real case study is investigated to compare the SSH response to different storm surge processes. The effect of wind (Figure 10a) is the largest compared to the effect of precipitation and the inverse barometer effect. It drives positive and negative SSH anomalies based on the wind direction and the geometry of the coastline. On 21 April 2006, the strong easterly wind to the south of the domain generates a positive surge at the western boundary of the Gulf of Carpentaria due to the onshore wind. A negative surge is generated at the south-eastern boundary of the gulf due to the offshore wind. On 22 April 2006, the easterly wind to the south of the domain continues to generate a positive and negative surge at the western and south-eastern boundaries of the gulf respectively. There is a SSH depression in the middle of the gulf due to Ekman pumping. This SSH depression is present in all the 6-hourly output from 1800 UTC 21 April 2006 to 1800 UTC 22 April 2006 when Monica is trekking across the Gulf of Carpentaria. The SSH depression is absent on 21 April 2006 and 23 April 2006 when the cyclone is near Cape York Peninsula and the Wessel Islands respectively. On 23 April 2006, the cyclone is relatively far from the eastern boundary of the gulf and the offshore winds here weakens from the range of 15 m s^{-1} (21 April 2006) to the range of 10 m s^{-1}. The negative surge at the eastern boundary of the gulf weakens correspondingly. On the other hand, the positive surge at the western boundary of the gulf strengthens with the strong onshore winds. At this time, the strong winds blowing into Buckingham Bay create a funnelling effect, channelling water into the bay and generating a high positive surge of up to 171 cm.

The SSH response to the inverse barometer effect is spatially constrained by the location of the cyclone's low pressure centre and varies in magnitude based on the storm intensity (Figure 10b). SSH is expected to increase by 1 cm for every 1 mbar drop in atmospheric pressure (Roden & Rossby, 1999). The inverse barometer effect contributes substantially to the storm surge when the low pressure centre of the cyclone coincides with the coastline. When the cyclone is away from the coastline and over the open sea, the inverse barometer effect raises the SSH but does not contribute significantly to the storm surge. On 21 April 2006, Monica crosses the west coast of Cape York Peninsula but due to its low intensity at this time, the contribution to the storm surge is only up to 13 cm. On 22 April 2006, the storm intensifies as it crosses the Gulf of Carpentaria but due to its distance from the coast, the contribution to the storm surge is only around 10 cm, despite raising the SSH up to 35.2 cm in the centre of the gulf. On 23 April 2006, Monica intensifies further, crossing the Wessel Islands and increases the storm surge by up to 61.5 cm.

A region is subjected to rain stress when rainfall and winds coincide. On 21 April 2006, the location of intense rain is situated just off the west coast of Cape York Peninsula (Figure 10c). The cyclone is traversing westward with an overall westward wind direction. Rain stress perturbation on the sea surface creates a positive front ahead of the perturbation and a negative front behind it as shown in Figure 4. The offshore winds and high rainfall at the eastern boundary of the gulf generates a SSH response to rain stress, enhancing the negative surge here. While the wind stress generated positive and negative surges at the western and south-eastern boundaries of the Gulf of Carpentaria, these surges are absent in the rain stress effect shown here due to the lower rainfall at these locations. On 22 April 2006, the cyclone is in the middle of the gulf trekking westwards. This creates a similar effect with the positive SSH ahead of the cyclone and a negative SSH behind it. The positive and negative surges at the western and south-eastern boundaries of the gulf are similarly absent here, due to the light rainfall in these areas. On 23 April 2006 when the cyclone crosses the Wessel Islands, the effect of rain stress is very similar to that of wind stress, with the intense rain coinciding with the strong winds here. The additional positive surge in Buckingham Bay is generated due to rain stress channelling water into the bay, which is similar to the effect of wind stress. At the northern coast of the Arnhem Land just west of the Wessel Islands, the offshore winds coincide with the high rainfall from the storm to generate an offshore rain stress and a negative surge of up to -2.9 cm.

Figure 10d shows the SSH response to precipitation mass addition. From 21 April 2006 to 22 April 2006, the areas of SSH change do not confine solely to the precipitation footprint (as traced out in Figure 8a), but spreads out, advecting to the south of the Gulf of Carpentaria. On 23 April 2006, the cyclone crosses the Wessel Islands and the rain mass is trapped in Buckingham Bay, generating an additional local SSH increase of 6.4 cm. The effect of precipitation is essentially an in-situ addition of mass, and inlets and semi-enclosed basins will serve to enhance this effect by trapping the rain. Buckingham Bay is fairly well-resolved in this 6 km resolution model, spanning 13 x 14 grid cells, so the size of the effect is unlikely to be just numerical. The geometry of the gulf itself is an important contributing factor towards the effect of precipitation seen here. From Figure 10d, it can be seen that the SSH response is generally higher to the southern half of the gulf than the north. If the gulf was entirely enclosed, the additional mass will be expected to distribute evenly by the clockwise gyre in both the northern and southern regions. The constrained southern boundary of the gulf enhances the build-up of SSH within the gulf, since the north-western section of the gulf opens up to the Arafura Sea. Typical remote enhancements are of the order of 2 cm.

Evaporation, often considered in tandem with precipitation, can have notable effects on sea surface elevation. Roden et al. (1999) have reported oceanic evaporation to be between 0.08 cm day^{-1} to 0.55 cm day^{-1}, depending on wind conditions. Hurricane evaporation rates have been found to be in the order of 1 – 2 cm day^{-1} (Riehl and Malkus (1958), Machta (1968), etc). At this order of magnitude, the evaporation rate is much smaller compared to the effect of rainfall in this case, with local effects of up to 14 cm (mass and momentum transfer). Nevertheless, it will be interesting to include the effect of evaporation rate on sea surface height in future work for a comprehensive comparison.

The Gulf of Carpentaria is not an isolated case of a semi-enclosed basin that is prone to severe storms and many other cases have been studied. Zhong et al. (2010) used ROMS to study the storm surge predictions during the passage of Hurricane Isabel in Chesapeake Bay and found that the hurricane translation speed and the resolution of the horizontal wind field are important factors affecting storm surges. Rego et al. (2010) used FVCOM to simulate Hurricane Ike at Galveston Bay and found that the Bolivar Peninsula provided a significant surge barrier in protecting the bay. Westerink et al. (2008) developed a model of south

Louisiana (which included many inlets, bays and channels) using ADCIRC to simulate the effect of storm surges during the events Hurricane Betsy and Andrew. Weisberg et al. (2006) used FVCOM to simulate the storm surge produced from several idealized hurricanes crossing Tampa Bay and found that the hurricanes with slow transitional speeds produced larger surges within the bay. However, none of these studies or models include the effect of rain mass. The semi-enclosed bay comprising Buckingham Bay, extending to the Wessel Islands and Gove Peninsula (12°2'S 136°5'E) consists of about 250 cells, which is equivalent to an area of 9000 km^2. The areas investigated in literature, such as Tampa Bay (5700 km^2), Galveston Bay (1600 km^2) and Chesapeake Bay (11600 km^2) are all of similar sizes or smaller. Not including the effect of rain mass in the models used in these studies will imply a systematic error in the storm surge levels modelled.To further compare how each of the physical effects contribute to coastal impacts in a worst case scenario, the SSH at the coastline starting from the Wessel Islands and ending at the northern tip of Cape York Peninsula is investigated. The maximum storm surge (for the duration of the storm) due to each physical effect is shown against the coastal locations (Figure 11) to illustrate the worst case scenario that can arise from each effect during this event. Considering the maximum storm surge response to the different processes at each coastal point, the additional effect of rain mass ranges from 1.3 cm to 6.4 cm, the effect of rain stress is from 0.4 cm to 7.5 cm, the inverse barometer effect is from 0.2 cm to 45.4 cm and the effect of wind stress is from 20.5 cm to 170.6 cm. While the inverse barometer effect is generally larger than the effect of rain mass, it falls below the effect of rain mass at the southern boundary of the gulf (coastal points 180 – 330) when the cyclone is located away from the coastline. This shows that the effect of rain mass can have a stronger remote presence than the inverse barometer effect. Although the maximum surge level due to the effect of rain stress is higher than the effect of rain mass, the effect of rain mass is larger than the effect of rain stress in most of the coastal points.

ROMS (and many ocean models) include the effect of rain stress but not the rain mass even when the effect of rain mass can be larger as shown here. Ocean models that consider the effect of rain stress to be sufficiently substantial to include its effect should not neglect the effect of rain mass.

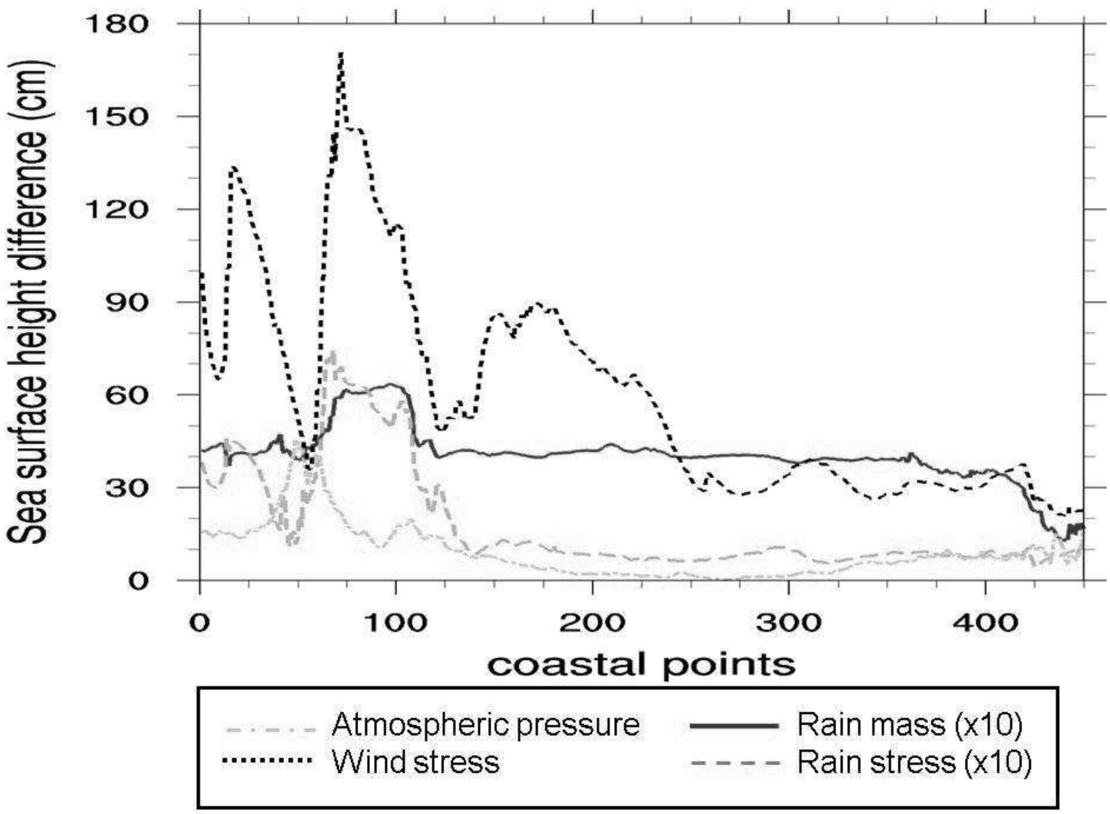

Figure 11: Comparison of the SSH change due to various physical effects, along the coastline at Gulf of Carpentaria. The coastal points can be attributed to different locations along the coastline as follows: the Wessel Islands (points 1 – 120), the western boundary of the Gulf of Carpentaria (points 121 – 180), the southern boundary of the gulf (points 181 – 280) and the eastern boundary of the gulf (points 281 – 450). SSH responses to rain mass and rain stress are scaled up by a factor of 10 for illustration.

5 Conclusion

Having successfully incorporated a new rain scheme into ROMS that considers the mass contribution of rainfall, its effect is shown in several cases. This new rain scheme does not interfere with the existing temperature and salinity treatment of rainfall in ROMS. The added rain mass generated surface waves that increase in propagation speed with increasing depth. An error in the existing implementation of rain stress in ROMS produced a systematic overestimation of 41% in magnitude and up to 45° in direction. This error has been corrected in this study and its isolated effect on SSH in a tropical cyclone case is shown in an idealized set-up. Finally, the effect of rain mass and rain stress in a real storm surge case (Cyclone Monica) is compared with the effect of winds and atmospheric pressure. In this case, the effect of wind and pressure generated a surge of up to 170.6 cm and 61.5 cm respectively. The effect of rain mass increases the SSH up to 6.4 cm in Buckingham Bay. The effect of rain mass has a stronger remote presence compared to the effect of pressure and rain stress. Especially in semi-enclosed areas, the effect of rain mass can substantially contribute to the storm surge even when the storm is relatively far from the coastline, and both the effect of pressure and rain stress are no longer significant. An area is subjected to high rain stress when intense winds coincide with heavy rain. Here, the effect of rain stress increases the SSH up to 7.5 cm, but the effect is generally smaller than the effect of rain mass along the coast. Many ocean models ignore the mass effect of rainfall and only incorporate the effect of wind, atmospheric pressure and rain stress. However, this study shows that the effect of rain mass can be larger than the effect of pressure and rain stress in certain scenarios, and should not be neglected. Each process shows different spatial influence and cannot be accounted for by simply scaling up a certain effect, for example, recalibrating the surge model by scaling the wind field.

References

Bleck, R., & Boudra, D. B. (1981). Initial Testing of a Numerical Ocean Circulation Model Using a Hybrid (Quasi-Isopycnic) Vertical Coordinate. *Journal of Physical Oceanography, 11*(6), 755-770. doi: Doi 10.1175/1520-0485(1981)011<0755:Itoano>2.0.Co;2

Caldwell, D. R., & Elliott, W. P. (1970). Surface stresses produced by rainfall. *J. Phys. Oceanography, 1*, 145-148.

Chapman, D. C. (1985). Numerical treatment of cross-shelf open boundaries in a barotropic coastal ocean model. *Journal of Physical Oceanography, 15*(8), 1060-1075. doi: 10.1175/1520-0485(1985)015<1060:ntocso>2.0.co;2

Chen, C. S., Qi, J. H., Li, C. Y., Beardsley, R. C., Lin, H. C., Walker, R., & Gates, K. (2008). Complexity of the flooding/drying process in an estuarine tidal-creek salt-marsh system: An application of FVCOM. *Journal of Geophysical Research-Oceans, 113*(C7). doi: Artn C07052 Doi 10.1029/2007jc004328

Chou, M, & Suarez, and M. J. (1994). An efficient thermal infrared radiation parameterization for use in general circulation models. *NASA Tech. Memo., 104606*(3), 85pp.

Clayson, C. A., & Kantha, L. H. (1999). Turbulent kinetic energy and its dissipation rate in the equatorial mixed layer. *Journal of Physical Oceanography, 29*(9), 2146-2166. doi: Doi 10.1175/1520-0485(1999)029<2146:Tkeaid>2.0.Co;2

Codiga, D.L. (2011). Unified Tidal Analysis and Prediction Using the UTide Matlab Functions. *Technical Report 2011-01 Graduate School of Oceanography, University of Rhode Island, Narragansett, RI. 59pp*

Dodla, V. B., Desamsetti, S., & Yerramilli, A. (2011). A Comparison of HWRF, ARW and NMM Models in Hurricane Katrina (2005) Simulation. *International Journal of Environmental Research and Public Health, 8*(6), 2447-2469. doi: DOI 10.3390/ijerph8062447

Dudhia, J. (1989). Numerical Study of Convection Observed during the Winter Monsoon Experiment Using a Mesoscale Two-Dimensional Model. *Journal of the Atmospheric Sciences, 46*(20), 3077-3107. doi: Doi 10.1175/1520-0469(1989)046<3077:Nsocod>2.0.Co;2

Dudhia, Jimy. (1996). A multi-layer soil temperature model for MM5. *Sixth PSU/NCAR Mesoscale Model Users' Workshop*.

Durden, S. L. (2010). Remote Sensing and Modeling of Cyclone Monica near Peak Intensity. *Atmosphere, 1*(1), 15-33. doi: Doi 10.3390/Atmos1010015

Egbert, G. D., Bennett, A. F., & Foreman, M. G. G. (1994). TOPEX/POSEIDON tides estimated using a global inverse model. *Journal of Geophysical Research-Oceans, 99*(C12), 24821-24852. doi: 10.1029/94jc01894

Fairall, C. W., Bradley, E. F., Rogers, D. P., Edson, J. B., & Young, G. S. (1996). Bulk parameterization of air-sea fluxes for Tropical Ocean Global Atmosphere Coupled Ocean Atmosphere Response Experiment. *Journal of Geophysical Research-Oceans, 101*(C2), 3747-3764. doi: Doi 10.1029/95jc03205

Flather, R. A. (1976). A tidal model of the northwest European continental shelf *Mémoires de la Société Royale de Sciences de Liege* (Vol. 6, pp. 141-164).

Gill, A. E., and P. P. Niiler (1973). The theory of the seasonal variability in the ocean, *Deep Sea Res.*, 20, 141-177

Griffies, S. M., & Hallberg, R. W. (2000). Biharmonic friction with a Smagorinsky-like viscosity for use in large-scale eddy-permitting ocean models. *Monthly Weather Review, 128*(8), 2935-2946.

Hirose, N., I. Fukumori, *and* R. M. Ponte (2001). A non-isostatic global sea level response to barometric pressure near 5 days, *Geophys. Res. Lett.,* 28, 2441–2444, *doi:*10.1029/2001GL012907.

Hong, S. Y., Noh, Y., & Dudhia, J. (2006). A new vertical diffusion package with an explicit treatment of entrainment processes. *Monthly Weather Review, 134*(9), 2318-2341. doi: Doi 10.1175/Mwr3199.1

Huffman, G. J., Adler, R. F., Bolvin, D. T., Gu, G. J., Nelkin, E. J., Bowman, K. P., . . . Wolff, D. B. (2007). The TRMM multisatellite precipitation analysis (TMPA): Quasi-global, multiyear, combined-sensor precipitation estimates at fine scales. *Journal of Hydrometeorology, 8*(1), 38-55. doi: Doi 10.1175/Jhm560.1

Janjic, Z. I. (1994). The Step-Mountain Eta Coordinate Model - Further Developments of the Convection, Viscous Sublayer, and Turbulence Closure Schemes. *Monthly Weather Review, 122*(5), 927-945. doi: Doi 10.1175/1520-0493(1994)122<0927:Tsmecm>2.0.Co;2

Jarvinen, B. R., & Lawrence, M. B. (1985). An Evaluation of the Slosh Storm-Surge Model. *Bulletin of the American Meteorological Society, 66*(11), 1408-1411.

Kain, J. S. (2004). The Kain-Fritsch convective parameterization: An update. *Journal of Applied Meteorology, 43*(1), 170-181. doi: Doi 10.1175/1520-0450(2004)043<0170:Tkcpau>2.0.Co;2

Lin, Y. L., Farley, R. D., & Orville, H. D. (1983). Bulk Parameterization of the Snow Field in a Cloud Model. *Journal of Climate and Applied Meteorology, 22*(6), 1065-1092. doi: Doi 10.1175/1520-0450(1983)022<1065:Bpotsf>2.0.Co;2

Machta, L. (1969). Evaporation rates based on tritium measurements for hurricane Betsy. *Tellus*, *21*(3), 404-408.

Marchesiello, P., McWilliams, J. C. , & Shchepetkin, A. F. . (2001). Open boundary conditions for long-term integration of regional ocean models. *Ocean Modelling, 3*, 1-20.

Mlawer, E. J., Taubman, S. J., Brown, P. D., Iacono, M. J., & Clough, S. A. (1997). Radiative transfer for inhomogeneous atmospheres: RRTM, a validated correlated-k model for the longwave. *Journal of Geophysical Research-Atmospheres, 102*(D14), 16663-16682. doi: Doi 10.1029/97jd00237

Paulson, C. A. (1970). The mathematical representation of wind speed and temperature profiles in the unstable atmospheric surface layer. *J. Appl. Meteor., 9*, 857–861.

Peng, M. C., Xie, L., & Pietrafesa, L. J. (2004). A numerical study of storm surge and inundation in the Croatan-Albemarle-Pamlico Estuary System. *Estuarine Coastal and Shelf Science, 59*(1), 121-137. doi: DOI 10.1016/j.ecss.2003.07.010

Pickard, G. L., & Emery, W. J. (1990). *Descriptive physical oceanography: an introduction*. Elsevier.

Ponte, R. M. (2006). Oceanic response to surface loading effects neglected in volume-conserving models. *Journal of Physical Oceanography, 36*(3), 426-434. doi: 10.1175/Jpo2843.1

Rego, J. L., & Li, C. Y. (2010). Storm surge propagation in Galveston Bay during Hurricane Ike. *Journal of Marine Systems, 82*(4), 265-279. doi: DOI 10.1016/j.jmarsys.2010.06.001

Riehl H, Malkus J. (2011). Some aspects of hurricane Daisy, 1958. *Tellus A* 13(2)

Roden, G. I., & Rossby, H. T. (1999). Early Swedish contribution to oceanography: Nils Gissler (1715-71) and the inverted barometer effect. *Bulletin of the American Meteorological Society, 80*(4), 675-682. doi: Doi 10.1175/1520-0477(1999)080<0675:Escton>2.0.Co;2

Rogers, Eric, , Thomas Black, , Brad Ferrier, , Ying Lin, , David Parrish, & , and Geoffrey DiMego. (2001). National Oceanic and Atmospheric Administration Changes to the NCEP Meso Eta Analysis and Forecast System: Increase in resolution, new cloud microphysics, modified precipitation assimilation, modified 3DVAR analysis. *NOAA*.

Saha, S., Moorthi, S., Pan, H. L., Wu, X. R., Wang, J. D., Nadiga, S., Goldberg, M. (2010). The Ncep Climate Forecast System Reanalysis. *Bulletin of the American Meteorological Society, 91*(8), 1015-1057. doi: Doi 10.1175/2010bams3001.1

Shchepetkin, A. F., & McWilliams, J. C. (2005). The regional oceanic modeling system (ROMS): a split-explicit, free-surface, topography-following-coordinate oceanic model. *Ocean Modelling, 9*(4), 347-404. doi: DOI 10.1016/j.ocemod.2004.08.002

Sheng, Y. P., Alymov, V., & Paramygin, V. A. (2010). Simulation of storm surge, wave, currents, and inundation in the Outer Banks and Chesapeake Bay during Hurricane Isabel in 2003: The importance of waves. *Journal of Geophysical Research-Oceans, 115*. doi: Artn C04008 Doi 10.1029/2009jc005402

Sheng, Y. P., Davis, J. R., Figueiredo, R., Liu, B., Liu, H., Luettich, R., Zheng, L. (2012). A regional testbed for storm surge and coastal inundation models - an overview. *Estuarine and Coastal Modeling, American Society of Civil Engineers*, 476-495.

Skamarock, W. C, Klemp, J. B, Dudhia, J, Gill, D. O, Baker, D. M, Duda, M. G, JG., Power. (2008). A Description of the Advanced Research WRF Version 3. . *NCAR/TN-475+STR*.

Smith, W. H. F., and Sandwell D. T. . (1997). Global seafloor topography from satellite altimetry and ship depth soundings. *Science, 277*, 1957-1962.

Stewart, Robert H. (2009). Introduction to Physical Oceanography. *University Press of Florida*.

Umlauf, L., & Burchard, H. (2003). A generic length-scale equation for geophysical turbulence models. *Journal of Marine Research, 61*(2), 235-265. doi: 10.1357/002224003322005087

Van Dorn, W. G. (1953). Wind stress on an artificial pond. *Journal of marine research, 12*, 249-276.

Wang, Shuai, Toumi, Ralf, Czaja, Arnaud, & Van Kan, Adrian. (2015). An Analytic Model of Tropical Cyclone Wind Profiles. *Quarterly Journal of the Royal Meteorological Society*, n/a-n/a. doi: 10.1002/qj.2586

Watson, P. J. (2011). Is There Evidence Yet of Acceleration in Mean Sea Level Rise around Mainland Australia? *Journal of Coastal Research, 27*(2), 368-377. doi: Doi 10.2112/Jcoastres-D-10-00141.1

Weisberg, R. H., & Zheng, L. Y. (2006). Hurricane storm surge simulations for Tampa Bay. *Estuaries and Coasts, 29*(6A), 899-913.

Westerink, J. J., Luettich, R. A., Baptista, A. M., Scheffner, N. W., & Farrar, P. (1992). Tide and Storm-Surge Predictions Using Finite-Element Model. *Journal of Hydraulic Engineering-Asce, 118*(10), 1373-1390. doi: Doi 10.1061/(Asce)0733-9429(1992)118:10(1373)

Westerink, J. J., Luettich, R. A., Feyen, J. C., Atkinson, J. H., Dawson, C., Roberts, H. J., Pourtaheri, H. (2008). A basin- to channel-scale unstructured grid hurricane storm surge model applied to southern Louisiana. *Monthly Weather Review, 136*(3), 833-864. doi: Doi 10.1175/2007mwr1946.1

Wu, C. C. (2013). TYPHOON MORAKOT Key Findings from the Journal TAO for Improving Prediction of Extreme Rains at Landfall. *Bulletin of the American Meteorological Society, 94*(2), 155-160. doi: Doi 10.1175/Bams-D-11-00155.1

Zhong, L. J., Li, M., & Zhang, D. L. (2010). How do uncertainties in hurricane model forecasts affect storm surge predictions in a semi-enclosed bay? *Estuarine Coastal and Shelf Science, 90*(2), 61-72. doi: DOI 10.1016/j.ecss.2010.07.001